The Astrophysical Journal Supplement Series, 265:10 (20pp), 2023 March https://doi.org/10.3847/1538-4365/acac8c

Simultaneous Time-monitoring Observations of H_2O and SiO Masers toward the Supergiant VX Sagittarii

Dong-Hwan Yoon[1], Se-Hyung Cho[1,2], Haneul Yang[1], Youngjoo Yun[1], and Jaeheon Kim[1]
[1] Korea Astronomy and Space Science Institute, 776 Daedeok-daero, Yuseong-gu, Daejeon, Republic of Korea; cho@kasi.re.kr
[2] Seoul National University, 1, Gwanak-ro, Gwanak-gu, Seoul, Republic of Korea
Received 2022 August 23; revised 2022 December 9; accepted 2022 December 15; published 2023 February 21

Abstract

We performed simultaneous monitoring observations of the 22.2 GHz H_2O and 43.1/42.8/86.2/129.3 GHz SiO masers toward the red supergiant VX Sagittarii using the Korean VLBI Network single-dish telescopes. The observations were conducted about every 2 months from 2013 May to 2019 January (30 epochs in total). They included four optical maxima in the active phase of the optical pulsation cycles. The line profile of a H_2O maser always comprised various velocity components with a wider velocity range and varied from highly redshifted to blueshifted velocities with respect to the stellar velocity, in contrast to those of the SiO masers. We examined the relation between peak intensities and velocities of 11 detailed components in the line profile of the H_2O maser and the pulsation phases. The peak intensity of each component generally exhibited a better correlation with the pulsation phases than that of total intensity. The peak velocities of several components gradually decreased or increased with respect to the stellar velocity, implying an accelerating motion and the development of asymmetries in the H_2O maser region. The characteristics of four transition SiO maser properties were compared according to the stellar pulsation phases. The intensity and velocity variation trend of the 43.1 GHz SiO maser was similar to that of the 42.8 GHz SiO maser. However, the variation trend of the 43.1 and 42.8 GHz SiO masers was different from that of the 86.2 and 129.3 GHz SiO masers. This difference stems from the different location of each maser reflecting a different excitation condition.

Unified Astronomy Thesaurus concepts: Circumstellar masers (240); Interstellar masers (846); Water masers (1790); A supergiant stars (8); Radio astrometry (1337); Single-dish antennas (1460); Silicon monoxide masers (1458)

Supporting material: extended figure

1. Introduction

The red supergiant VX Sagittarii (VX Sgr) is in an important period in the late evolutionary phase of a massive star with a high mass-loss rate and luminosity. However, it was suggested to be an extreme asymptotic giant branch (AGB) based on the Mira-like behavior and the RbI lines (Tabernero et al. 2021). Its optical variable type is semiregular with an average period of 732 days, which somewhat varies depending on the time (Lockwood & Wing 1982; Samus et al. 2017). Its mass is about 12 $M_\odot$ (Chiavassa et al. 2010), the luminosity is about 1.95×10^5 $L_\odot$ (Xu et al. 2018), and the accompanying mass-loss rate is $\sim 10^{-5}$ $M_\odot$ yr^{-1} (Chapman & Cohen 1986). Its distance is measured to be 1.57 kpc through the proper motion of the SiO masers (Chen et al. 2007). The stellar and expansion velocities are measured to be ∼5.3 and ∼20 km s^{-1}, respectively, using the double peaks of the OH maser (Chapman & Cohen 1986). Additionally, its spectral type varies from M4eIa to ∼M10eIa, and the corresponding apparent magnitude is between about 14 and 6.5 mag (Kiss et al. 2006; Samus et al. 2009).

Furthermore, VX Sgr is a well-known emitter of strong SiO, H_2O, and OH masers. Owing to their stratified distributions according to different excitation conditions, these masers are useful probes for investigating the structure and kinematics from the atmosphere close to the central star to the outer envelope of the star. In particular, their intensities and line profiles are highly variable, and they provide good information on the effects of stellar pulsations. Time-monitoring observations toward VX Sgr with the 13.7 m radio telescope of the Centro Astronomico de Yebes exhibit that the intensity variations of the SiO $v = 1$, 2, $J = 1$–0 masers are generally well correlated with the optical curve and line profiles, comprising six or seven peaks at velocities between −5 and +20 km s^{-1} and showing very complex features (Alcolea et al. 1999). Pardo et al. (2004) reported that the main feature in the intensity variations of SiO masers is a secular weakening. The high-resolution observations of the SiO $v = 1$, $J = 1$–0 maser with the Very Long Baseline Array (VLBA) have revealed a ringlike distribution of SiO masers with a radius of ∼3 stellar radii and an angular size of 0.5 mas for individual maser features (Chen et al. 2006). Su et al. (2018) suggested that the SiO maser shell expands in a decelerating manner, and the maser spot's motion reflects the real gas stream rather than the changes in physical conditions.

Gomez Balboa & Lepine (1986) and Berulis et al. (1999) conducted time-monitoring observations of the 22 GHz H_2O maser toward VX Sgr using a single-dish telescope. Gomez Balboa & Lepine (1986) determined the coincidence between the maximum of the H_2O maser intensity and that of the optical magnitude. Berulis et al. (1999) suggested that the H_2O maser stems from the circumstellar disk and bipolar outflows. Based on the very long baseline interferometry (VLBI) observations of the H_2O maser using MERLIN, Murakawa et al. (2003)

suggested a spheroidal thick shell model with accelerating stellar wind. Vlemmings et al. (2005), through the H_2O maser polarization observations with the VLBA, stated that the coupling between the stellar outflow and the magnetic field could cause an asymmetric mass loss.

However, the above studies were inevitably conducted as separate observational studies for the SiO and H_2O masers due to the lack of a simultaneous observation system of both SiO and H_2O masers. Recently, the Korean VLBI Network (KVN) has enabled us to implement the KVN Key Science Program (KSP) of evolved stars (https://radio.kasi.re.kr/kvn/ksp.php; Cho et al. 2018), which simultaneously observes the 43.1/42.8/86.2/129.3 GHz SiO and 22.2 GHz H_2O masers with both the single-dish and VLBI systems. Yoon et al. (2018) presented the pilot KSP VLBI results for VX Sgr, which show that a nearly circular structure traced by the multitransition SiO masers develops into a highly asymmetric structure traced by a H_2O maser through the dust layers. The simultaneous monitoring observations of the SiO and H_2O masers using the KVN single-dish telescope complement the KVN VLBI results. Moreover, VX Sgr has quiet or active long-period phases with a small and large amplitude of visual-magnitude variations (Kamohara et al. 2005). Observations at a specific period are limited to a comprehensive analysis, such as long-term pulsation, atmospheric variations, and mass-loss trends in VX Sgr. Therefore, the systematic monitoring observations of both SiO and H_2O masers that cover several periods can depict the influence from the stellar atmosphere to the circumstellar envelope above dust layers on the maser properties according to semiregular pulsations. Using the KVN single-dish telescope, we performed simultaneous monitoring observations of the SiO and H_2O masers in 30 epochs over 3.5 periods from 2013 May to 2019 January during the active phase.

The observations and data reduction are given in Section 2, and an overview of the observational results, including each spectrum, is given in Section 3. Analyses of maser properties according to the observational epochs are presented in Section 4. Discussion and summary are presented in Sections 5 and 6, respectively.

2. Observations and Data Reduction

Using the three KVN 21 m single-dish telescopes located at the Yonsei University campus in Seoul, the Ulsan University campus in Ulsan, and the Tamna University campus in Jeju (marked as KYS, KUS, and KTN, respectively, in Table 1), we performed simultaneous monitoring observations of the H_2O $6_{1,6}$–$5_{2,3}$ (22.235080 GHz), SiO $v = 1, 2$, $J = 1$–0 (43.122080 and 42.820587 GHz), SiO $v = 1$, $J = 2$–1 (86.243442 GHz), and SiO $v = 1$, $J = 3$–2 (129.363359 GHz) maser lines. The observations were conducted every 2 months from 2013 May to 2019 January in a total of 30 epochs (blue triangles in Figure 1). The half-power beam widths and the aperture efficiencies for each band were 126″, 0.59 (at the K band; 22.2 GHz), 63″, 0.63 (at the Q band; 43.1 GHz), 32″, 0.56 (at the W band; 86.2 GHz), and 23″, 0.41 (at the D band; 129.3 GHz) during our observation period.[3]

The KVN antennas were designed to be shaped-Cassegrain type with quasi-optics for multifrequency observations. The quasi-optics system splits a signal from the subreflector into four $K/Q/W/D$-band receivers using three dichroic low-pass filters (Han et al. 2008). The system temperature ranged from 80 to 200 (K band), 130 to 250 (Q band), 150 to 470 (W band), and 210 to 820 (D band) K, depending on the receiver and weather conditions. We used a digital spectrometer with a set of total bandwidths of 32 MHz for the K and Q bands and 64 MHz for the W and D bands. These bandwidths correspond to the radial velocity ranges of 440 (K band), 220 (Q band), 220 (W band), and 110 (D band) km s^{-1}. The velocity resolution through Hanning smoothing at K, Q, W, and D was about 0.21 km s^{-1}.

The observations were performed in the position-switching mode, and the integration time was 90–120 minutes to achieve an rms sensitivity of 0.01–0.05 K. The chopper wheel method was used as a basic calibration to correct for the atmospheric uncertainty. This method was employed along with the sky dip curve fit to measure the atmospheric attenuation, antenna gain fluctuations, and atmospheric opacity to the target direction. Only left-polarized data were used. The pointing was checked using the 86.2 GHz SiO maser from VX Sgr itself. The average values of the conversion factors representing the ratio between the antenna temperature and flux density were 13.6 ± 0.8, 12.9 ± 0.3, 15.6 ± 0.7, and 22.1 ± 2.4 Jy K^{-1} at 22.2, 43.1, 86.2, and 129.3 GHz for the three KVN telescopes, respectively.

Data processing was performed using the CLASS software in the GILDAS package.[4] This software measures the intensity and velocity variations of a spectrum through accurate baseline fitting. Table 1 summarizes the detailed observational information.

3. Observational Results

Figure 2 displays the simultaneously obtained monitoring spectra of the 22.2 GHz H_2O ($6_{1,6}$–$5_{2,3}$) and 43.1 GHz SiO ($v = 1$, $J = 1$–0), 42.8 GHz SiO ($v = 2$, $J = 1$–0), 86.2 GHz SiO ($v = 1$, $J = 2$–1), and 129.3 GHz SiO ($v = 1$, $J = 3$–2) masers with the KVN single-dish telescopes for 30 epochs from 2013 May to 2019 January. For simplicity of notation, each maser is denoted as a frequency instead of a transition from here. The spectra in the 129.3 GHz SiO maser of 2014 August 27 and 2015 August 17 were not obtained due to D-band receiver maintenance. In Figure 2, the red dotted lines represent the stellar velocity of VX Sgr, $V_{LSR} = 5.3$ km s^{-1} (Chapman & Cohen 1986). Hereafter, the stellar velocity $V_{LSR} = 5.3$ km s^{-1} is denoted as $V_* = 5.3$ km s^{-1}. The optical phases were calculated based on the four optical maxima in Figure 1 during our monitoring observations. Since the optical pulsation period varies, we set the pulsation period from the optical maximum according to each observation date to the next optical maximum and divided the phases from zero to 1 based on the determined period. The optical magnitude reached its maximum value four times during the observations. The interval of each cycle corresponds to 658 (from the optical maximum of 2013 to that of 2015), 583 (from the optical maximum of 2015 to that of 2017), and 517 (from the optical maximum of 2017 to that of 2018) days. The H_2O maser spectra comprised many components compared to those of the SiO masers and exhibited a broad velocity width. Furthermore, the peak components of the H_2O maser spectra exhibited a large blue or red velocity shift with respect to the stellar velocities compared to those of the SiO masers. The monitoring

[3] https://radio.kasi.re.kr/kvn/status_report_2019

[4] https://www.iram.fr/IRAMFR/GILDAS/

Table 1
The Results of the Single-dish Observation for H_2O and SiO Maser Lines

Molecular Transition (1)	Date (yymmdd) (2)	Optical Phase (ϕ) (3)	T_A^* (peak) (K) (4)	V_{LSR} (peak) (km s^{-1}) (5)	$\int T_A^* dv$ (K km s^{-1}) (6)	V_{LSR} (mean) (km s^{-1}) (7)	rms (K) (8)	Telescope (Site) (9)
H_2O	130505	−0.05	43.86	5.9	316.41	5.6	0.026	KTN
$6_{(1,6)}$–$5_{(2,3)}$	130916	0.16	58.44	5.9	393.07	6.7	0.028	KUS
	131125	0.26	61.77	5.9	408.69	5.2	0.026	KYS
	140211	0.38	46.58	5.8	332.09	6.1	0.015	KYS
	140406	0.46	41.45	5.9	335.46	4.0	0.020	KTN
	140605	0.55	33.05	5.8	313.51	4.6	0.066	KYS
	140827	0.68	42.72	−1.0	310.92	4.5	0.079	KUS
	141012	0.75	42.97	−0.9	325.57	4.0	0.061	KUS
	141219	0.85	28.17	5.9	271.14	4.4	0.029	KTN
	150209	0.93	31.14	5.9	302.24	4.2	0.019	KUS
	150417	1.04	27.29	5.4	272.37	4.4	0.018	KYS
	150610	1.13	33.28	5.4	335.46	4.8	0.032	KUS
	150817	1.25	29.93	5.7	295.85	4.3	0.064	KYS
	151005	1.33	34.26	5.4	358.89	6.9	0.025	KYS
	151213	1.45	37.37	−3.0	323.83	4.4	0.020	KUS
	160215	1.56	54.29	−3.0	330.29	7.3	0.016	KYS
	160405	1.65	60.33	−3.0	305.82	6.1	0.021	KUS
	160921	1.94	60.27	−3.0	287.04	4.0	0.032	KUS
	161120	2.04	67.74	−3.0	385.96	5.2	0.017	KUS
	170131	2.18	45.57	−3.0	373.93	5.2	0.019	KYS
	170415	2.33	30.99	−3.0	348.29	4.8	0.026	KYS
	170604	2.42	25.87	22.7	335.27	4.8	0.030	KUS
	170828	2.59	20.51	22.7	230.59	4.8	0.045	KUS
	171101	2.71	18.07	5.0	213.77	4.8	0.027	KUS
	180102	2.83	24.39	5.0	274.27	4.2	0.024	KTN
	180310	2.96	33.24	5.1	330.40	3.9	0.016	KYS
	180615	3.15	56.38	0.1	330.40	4.7	0.053	KYS
	180910	3.32	54.40	5.1	464.13	3.8	0.030	KTN
	181103	3.42	70.52	0.1	564.67	5.5	0.025	KTN
	190105	3.54	59.62	4.7	464.56	6.8	0.014	KYS
SiO	130505	−0.05	10.50	3.8	69.93	7.9	0.025	KTN
$v = 1$, $J = 1$–0	130916	0.16	13.21	4.3	89.14	7.7	0.020	KUS
	131125	0.26	14.86	3.8	95.79	6.6	0.027	KYS
	140211	0.38	10.35	3.4	71.63	7.7	0.017	KYS
	140406	0.46	8.58	3.9	66.08	6.6	0.021	KTN
	140605	0.55	7.99	2.1	71.65	6.8	0.031	KYS
	140827	0.68	7.71	3.4	53.88	7.1	0.029	KUS
	141012	0.75	7.03	3.8	50.29	7.3	0.029	KUS
	141219	0.85	7.19	2.1	52.36	7.5	0.028	KTN
	150209	0.93	7.37	5.2	54.89	6.4	0.014	KUS
	150417	1.04	12.94	5.6	84.60	6.9	0.022	KYS
	150610	1.13	15.89	3.0	82.37	6.6	0.015	KUS
	150817	1.25	7.75	4.3	55.06	8.2	0.028	KYS
	151005	1.33	9.45	4.7	70.01	5.8	0.022	KYS
	151213	1.45	8.85	3.8	66.05	5.6	0.018	KUS
	160215	1.56	7.99	4.3	64.74	6.0	0.021	KYS
	160405	1.65	4.40	8.2	46.17	4.7	0.018	KUS
	160921	1.94	5.41	7.8	41.90	6.9	0.023	KUS
	161120	2.04	7.24	6.5	49.43	5.6	0.017	KUS
	170131	2.18	11.35	9.5	70.57	6.3	0.019	KYS
	170415	2.33	9.45	4.8	71.81	8.0	0.021	KYS
	170604	2.42	15.10	4.8	81.94	6.1	0.021	KUS
	170828	2.59	10.89	8.2	69.51	6.4	0.022	KUS
	171101	2.71	12.28	7.3	74.09	7.8	0.018	KUS
	180102	2.83	11.61	6.0	75.25	6.4	0.019	KTN
	180310	2.96	17.83	7.7	98.06	6.4	0.013	KYS
	180615	3.15	23.11	6.9	108.13	8.2	0.024	KYS
	180910	3.32	13.10	7.3	86.85	7.3	0.017	KTN
	181103	3.42	14.20	7.3	102.34	6.6	0.018	KTN
	190105	3.54	13.65	8.2	104.40	7.5	0.014	KYS
SiO	130505	−0.05	5.93	3.8	27.89	6.2	0.025	KTN
$v = 2$, $J = 1$–0	130916	0.16	7.07	6.0	38.30	5.6	0.020	KUS

Table 1
(Continued)

Molecular Transition (1)	Date (yymmdd) (2)	Optical Phase (ϕ) (3)	T_A^* (peak) (K) (4)	$V_{\rm LSR}$ (peak) (km s^{-1}) (5)	$\int T_A^* dv$ (K km s^{-1}) (6)	$V_{\rm LSR}$ (mean) (km s^{-1}) (7)	rms (K) (8)	Telescope (Site) (9)
	131125	0.26	11.08	5.6	58.66	4.5	0.027	KYS
	140211	0.38	6.19	5.6	35.93	5.6	0.017	KYS
	140406	0.46	5.30	4.3	25.39	4.5	0.021	KTN
	140605	0.55	4.73	3.8	24.40	6.5	0.031	KYS
	140827	0.68	3.77	3.4	16.95	6.0	0.029	KUS
	141012	0.75	3.55	3.4	16.87	5.8	0.029	KUS
	141219	0.85	2.86	4.3	17.86	7.1	0.028	KTN
	150209	0.93	3.27	3.4	19.88	6.0	0.014	KUS
	150417	1.04	4.86	4.7	27.09	4.7	0.022	KYS
	150610	1.13	4.78	4.3	25.23	5.8	0.015	KUS
	150817	1.25	2.73	3.8	17.33	6.0	0.028	KYS
	151005	1.33	2.63	3.4	22.08	6.5	0.022	KYS
	151213	1.45	4.25	3.0	26.18	7.1	0.018	KUS
	160215	1.56	4.72	3.4	32.85	8.5	0.021	KYS
	160405	1.65	2.57	6.9	21.16	6.2	0.018	KUS
	160921	1.94	6.60	4.7	32.06	6.5	0.023	KUS
	161120	2.04	4.52	8.2	27.39	6.7	0.017	KUS
	170131	2.18	7.34	9.1	43.33	6.9	0.019	KYS
	170415	2.33	7.88	9.1	39.69	10.8	0.021	KYS
	170604	2.42	10.76	7.8	52.79	4.3	0.021	KUS
	170828	2.59	8.37	6.5	46.61	6.7	0.022	KUS
	171101	2.71	10.59	6.0	46.78	8.0	0.018	KUS
	180102	2.83	9.22	6.0	46.33	7.8	0.019	KTN
	180310	2.96	9.56	5.6	49.41	6.0	0.013	KYS
	180615	3.15	13.25	6.5	60.35	5.6	0.024	KYS
	180910	3.32	9.33	8.6	56.34	5.8	0.017	KTN
	181103	3.42	9.55	6.5	57.90	5.3	0.018	KTN
	190105	3.54	8.15	6.5	45.64	6.2	0.014	KYS
SiO	130505	−0.05	11.91	3.8	105.24	7.1	0.024	KTN
$v = 1$, $J = 2$–1	130916	0.16	17.57	4.7	132.28	8.4	0.039	KUS
	131125	0.26	15.92	2.1	149.27	7.7	0.039	KYS
	140211	0.38	10.32	5.2	94.02	7.1	0.019	KYS
	140406	0.46	10.91	5.5	88.19	5.6	0.020	KTN
	140605	0.55	11.99	5.6	100.64	7.3	0.058	KYS
	140827	0.68	14.03	5.1	94.10	6.0	0.060	KUS
	141012	0.75	17.52	5.1	128.38	3.6	0.066	KUS
	141219	0.85	17.16	3.4	114.51	5.1	0.036	KTN
	150209	0.93	14.83	2.1	118.52	6.0	0.021	KUS
	150417	1.04	27.55	4.7	176.88	7.5	0.024	KYS
	150610	1.13	26.03	4.7	162.35	6.9	0.024	KUS
	150817	1.25	8.22	3.9	56.77	7.1	0.042	KYS
	151005	1.33	15.90	4.7	114.68	5.8	0.025	KYS
	151213	1.45	10.69	4.7	110.36	3.9	0.022	KUS
	160215	1.56	12.67	4.7	87.11	3.8	0.019	KYS
	160405	1.65	12.01	4.7	83.30	4.1	0.023	KUS
	160921	1.94	16.26	4.7	84.84	7.3	0.040	KUS
	161120	2.04	11.07	4.7	63.53	7.0	0.017	KUS
	170131	2.18	10.13	5.1	76.10	9.0	0.021	KYS
	170415	2.33	6.27	3.8	55.90	5.6	0.025	KYS
	170604	2.42	7.06	2.9	61.79	5.8	0.035	KUS
	170828	2.59	5.07	4.7	46.68	5.3	0.053	KUS
	171101	2.71	5.34	5.6	49.39	6.2	0.027	KUS
	180102	2.83	4.78	3.0	39.56	7.7	0.019	KTN
	180310	2.96	6.48	2.5	48.60	6.4	0.020	KYS
	180615	3.15	10.11	1.6	81.29	6.9	0.052	KYS
	180910	3.32	6.02	6.0	54.75	7.6	0.023	KTN
	181103	3.42	9.89	6.4	88.36	6.4	0.018	KTN
	190105	3.54	10.27	6.9	89.24	5.8	0.015	KYS
SiO	130505	−0.05	3.99	4.1	25.47	8.8	0.018	KTN
$v = 1$, $J = 3$–2	130916	0.16	2.64	3.0	20.79	5.0	0.049	KUS
	131125	0.26	3.67	4.8	26.77	4.5	0.045	KYS
	140211	0.38	1.24	4.7	7.06	5.0	0.024	KYS

Table 1
(Continued)

Molecular Transition (1)	Date (yymmdd) (2)	Optical Phase (ϕ) (3)	T_A^* (peak) (K) (4)	V_{LSR} (peak) (km s^{-1}) (5)	$\int T_A^* dv$ (K km s^{-1}) (6)	V_{LSR} (mean) (km s^{-1}) (7)	rms (K) (8)	Telescope (Site) (9)
	140406	0.46	3.22	4.2	17.91	7.9	0.015	KTN
	140605	0.55	1.91	4.8	11.39	5.0	0.142	KYS
	140827	0.68	…	…	…	…	…	KUS
	141012	0.75	2.31	4.7	14.65	3.6	0.115	KUS
	141219	0.85	3.48	4.2	21.34	6.5	0.036	KTN
	150209	0.93	2.01	5.3	12.95	6.2	0.008	KUS
	150417	1.04	9.49	4.7	43.66	9.7	0.014	KYS
	150610	1.13	4.68	4.8	25.17	6.5	0.025	KUS
	150817	1.25	…	…	…	…	…	KYS
	151005	1.33	1.64	5.4	10.76	7.4	0.028	KYS
	151213	1.45	1.96	5.4	12.16	5.9	0.018	KUS
	160215	1.56	1.93	5.3	10.98	6.5	0.016	KYS
	160405	1.65	1.68	5.9	14.42	9.5	0.016	KUS
	160921	1.94	2.75	4.2	17.83	4.5	0.052	KUS
	161120	2.04	2.98	4.8	24.93	5.6	0.016	KUS
	170131	2.18	2.70	5.2	16.99	5.4	0.019	KYS
	170415	2.33	1.27	5.7	8.61	7.4	0.036	KYS
	170604	2.42	1.21	4.8	9.16	6.1	0.046	KUS
	170828	2.59	0.93	5.6	3.36	4.8	0.169	KUS
	171101	2.71	1.39	5.3	7.60	6.2	0.021	KUS
	180102	2.83	0.62	4.8	3.16	8.3	0.014	KTN
	180310	2.96	1.97	5.9	9.75	8.2	0.013	KYS
	180615	3.15	2.75	5.3	15.36	8.8	0.066	KYS
	180910	3.32	1.48	5.3	6.94	8.5	0.024	KTN
	181103	3.42	2.19	5.3	12.95	10.5	0.020	KTN
	190105	3.54	1.72	1.3	12.78	10.2	0.009	KYS

spectra of each H_2O and SiO maser line are presented according to the observational dates and epochs in Figures 3 and 4, respectively. The observed properties of the H_2O and SiO masers are summarized in Table 1, including optical phase, peak antenna temperature, peak velocity, integrated antenna temperature, and mean velocity.

In Figure 3, many components (more than eight) in the H_2O maser spectra span from ~ -10 to ~ 23 km s^{-1}. Highly redshifted components of the H_2O maser around 23 km s^{-1} are well developed over almost all of the observational epochs compared to the blueshifted components. These components exhibit the strongest intensity in 2017 June (22nd), as shown in Figure 2. Most blueshifted H_2O maser components around 3 km s^{-1} predominantly appeared from 2015 December (15th) to 2017 April (21st). The stellar velocity components around 5–6 km s^{-1} were dominant from 2013 May (1st) to 2015 October (14th) and from 2017 November (24th) to 2019 January (30th).

The SiO masers appeared around the stellar velocity and exhibited a relatively simple spectrum and small time variation compared to the H_2O masers (Figure 4). The overall features of the 43.1 GHz SiO maser spectra are similar to those of the 42.8 GHz SiO maser. The peak component variations of the 43.1 and 42.8 GHz SiO masers exhibited a similar trend; i.e., their peak components appeared around the blueshifted velocities with respect to the stellar velocity from 2013 to 2016, and they appeared around redshifted velocities from 2017 to 2019. Different from other epochs, the upper part of the 43.1 and 42.8 GHz SiO maser spectra was broad in 2016 April (17th), when the optical minimum had the lowest value among the three minimum values. In contrast, the peak components of the 86.2 and 129.3 GHz SiO masers appeared around the stellar velocity in most observational epochs. The weak redshifted component of the 43.1 GHz SiO maser appeared at about 20 km s^{-1} in 2013 May and 2013 September (1st and 2nd) but disappeared thereafter and reappeared from 2018 March (26th). For the 86.2 GHz SiO maser, the peak was blueshifted from 2017 April (21st) and then redshifted from 2018 September (28th). The 129.3 GHz SiO maser was the weakest among the observed four SiO masers, but it comprised various components. In particular, redshifted features near 14 km s^{-1} were observed from 2015 October (14th) to 2017 April (21st). According to the KVN VLBI observations in 2016 March (Yoon et al. 2018), they were located in the southern part of the star and were not associated with other SiO masers in terms of velocity and position.

4. Analyses of Maser Properties according to Observational Epochs

4.1. Time Variations of H_2O and SiO Maser Intensities

Figure 5 presents the peak and integrated antenna temperature variations with the AAVSO optical light curve. The blue and red triangles denote the single-dish and VLBI observation dates (D.-H. Yoon et al. 2023, in preparation), respectively. The red dashed lines represent the maximum of the optical magnitude during our observations. Object VX Sgr has a quiet or active long-period phase together with a small cycle of general pulsations (Kamohara et al. 2005). Kamohara et al. (2005) argued that the visual-magnitude variation was greater during the active phase ($\sim$6 mag) than the quiet phase ($\sim$2 mag). Our single-dish observations were performed in the active phase, which exhibited considerable magnitude and period variations. The interval of each optical maximum from

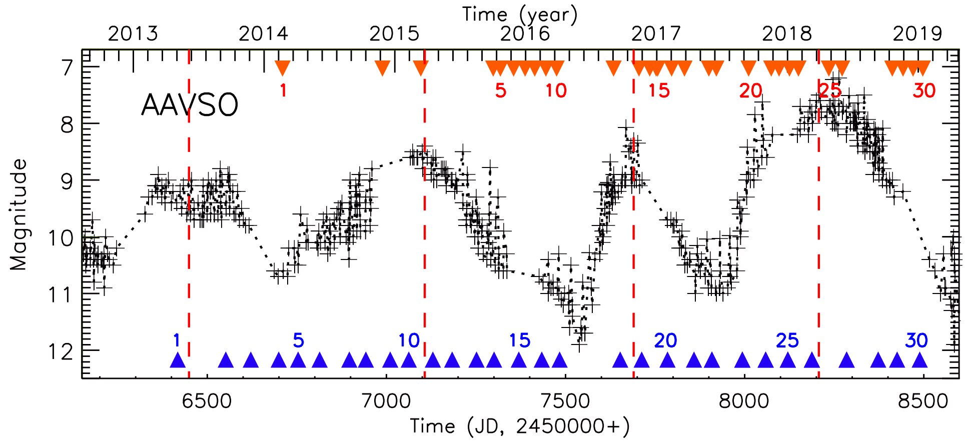

Figure 1. Optical magnitude variation of VX Sgr from AAVSO. The red dashed lines denote the optical maxima. The blue and red triangles correspond to the single-dish and VLBI observations, respectively. The numbers around the triangles indicate the order of observational epochs in the single-dish and VLBI observations.

the optical maximum of 2013 corresponded to 658, 583, and 517 days, showing a semiregular variable type.

Figure 5 presents the peak (panel (a)) and integrated (panel (b)) antenna temperature variations of the SiO masers related to the optical magnitude variations. The peak intensities of the 43.1, 42.8, and 86.2 GHz SiO masers reached their maxima at about 0.26 phase after the first optical maximum, except those of the 129.3 GHz SiO maser. The 43.1, 42.8, and 86.2 GHz SiO masers and the 129.3 GHz SiO maser exhibited their maxima a little after the second and fourth optical maxima. However, this tendency changes around the third optical maximum. The 43.1 and 42.8 GHz SiO masers did not exhibit their intensity maxima, in contrast to the 86.2 and 129.3 GHz SiO masers. Moreover, the 43.1 and 42.8 GHz SiO masers did not exhibit minimum intensities, in contrast to the 86.2 and 129.3 GHz SiO masers, and their intensities continued to increase to the fourth optical maximum. These different behaviors of the 43.1 and 42.8 GHz SiO masers may be associated with the different locations of the masers, the relatively low optical amplitude of the third optical maximum, and the rapid brightening during the short optical period of 517 days between 2017 and 2018, i.e., a variation of stellar pulsation motion.

The H_2O masers exhibited intensity maxima after the first, third, and fourth optical maxima. However, they did not exhibit the intensity maximum around the second optical maximum, in contrast to the SiO masers. In particular, the H_2O maser exhibited an intensity peak at the most redshifted velocity of 22.7 km s^{-1} (Figure 2) when the optical phase was minimum ($\phi = 2.42$) on 2017 June 4 (22nd) during the short optical period of 517 days. This intensity peak shows the local maximum of the H_2O maser on 2017 June 4 in Figure 5(a). The variation trends of the integrated antenna temperatures of the H_2O and SiO masers were similar to those of the peak antenna temperatures, as shown in Figure 5(b). However, the integrated antenna temperatures of the H_2O maser exhibited a small maximum after the second optical maximum, unlike the case of the peak antenna temperature.

4.2. Peak and Mean Velocity Variations of H_2O and SiO Maser Lines

Figure 6 shows the variations of the peak and mean velocities with respect to the stellar velocity ($V_* = 5.3$ km s^{-1}) according to the observation dates. The peak velocity is the velocity at the strongest intensity point in the maser spectrum after the polynomial baseline fitting, and the mean velocity is the emission-weighted velocity of the maser emission. A negative value of the velocity indicates a blueshift, and a positive value indicates a redshift with respect to the stellar velocity. The peak velocities of the 43.1 and 42.8 GHz SiO masers were dominated by blueshift until 2016 April (17th) and redshift thereafter (Figure 6(a)). The turning point from the blueshifted to redshifted velocities occurred around the rapid brightening phase of the optical magnitude from the optical minimum in 2016. Furthermore, the peak velocities of the 86.2 and 129.3 GHz SiO masers were dominated by blueshift during most of the monitoring period. These different behaviors of the peak velocities between the masers may be associated with their different locations (Yoon et al. 2018), as in the case of their peak intensities.

The peak velocities of the H_2O maser appeared at around the stellar velocities in many epochs. However, in 2017 May, the peak velocity of the H_2O maser episodically changed from blueshifted to redshifted velocities. We speculate that the abrupt dynamical changes around the optical minimum in 2016 affected the H_2O maser region. This is because the sharp increase in intensity more than doubled in the redshifted component at 22.7 km s^{-1} in the 22nd epoch. The location of the episodic variation in the position–velocity spot maps of VLBI monitoring data around the 17th–19th epochs needs to be verified. The peak velocities of the H_2O maser have a relatively constant value that differs from those of the SiO maser.

Figure 6(b) exhibits the mean velocity variations. The mean velocities of the SiO masers are dominant in the redshifted emission and exhibit large variations compared to those of the H_2O maser. These differences in the mean velocities between the H_2O and SiO masers may be associated with their different locations and pumping mechanisms. Namely, the SiO masers arise from the turbulent regions inside dust layers, while the H_2O maser arises from above the dust layers, where the outward motion accelerates close to the terminal velocity. As for the pumping mechanisms, both radiative and collisional pumping have been suggested for SiO masers (Lockett & Elitzur 1992; Bujarrabal 1994), while collisional pumping has been suggested for H_2O masers (Cooke & Elitzur 1985).

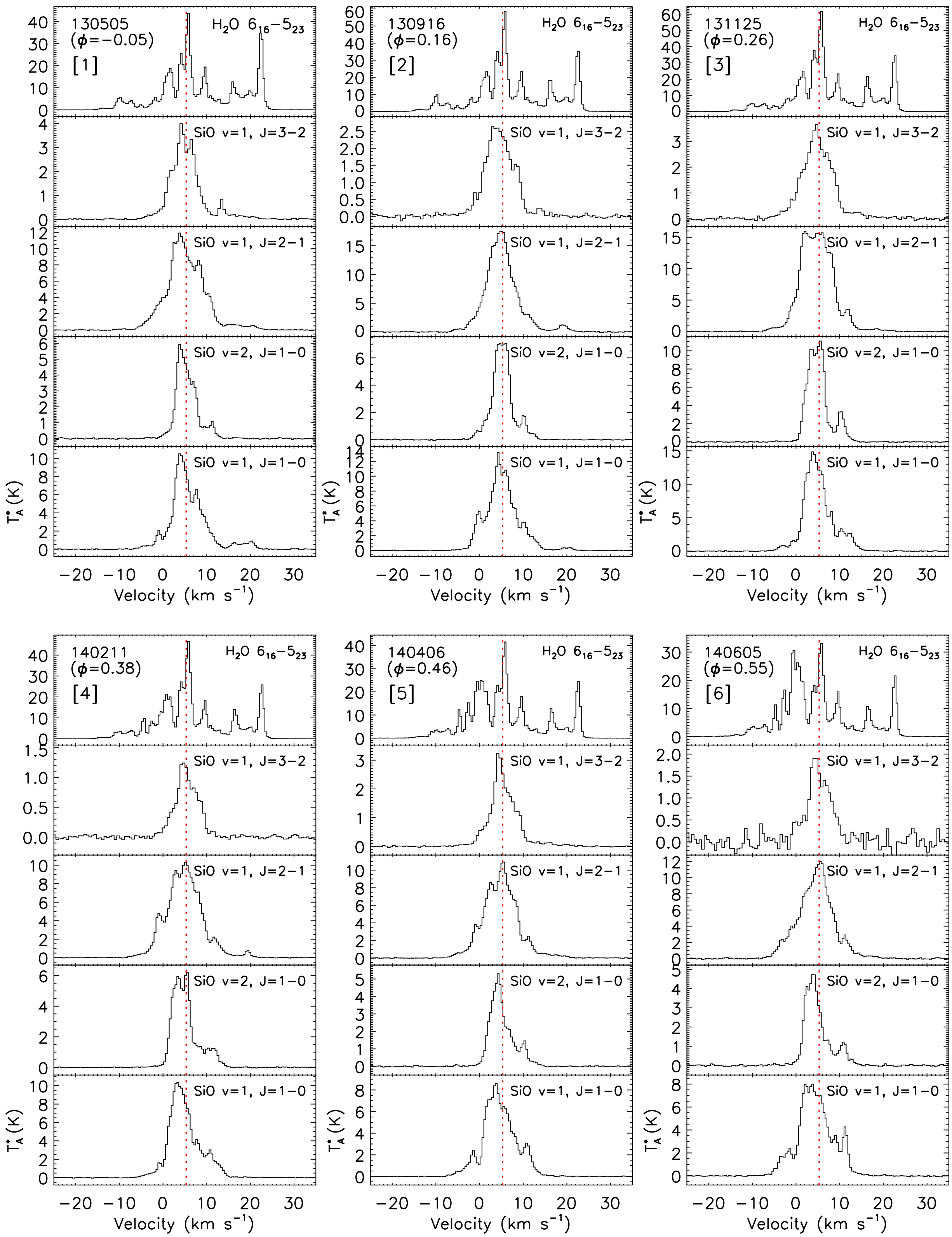

Figure 2. The H_2O and SiO maser spectra of VX Sgr in SiO $v = 1$, 2, $J = 1$–0; $v = 1$, $J = 2$–1, $J = 3$–2 (43.1, 42.8, 86.2, 129.3 GHz); and H_2O $6_{1,6}$–$5_{2,3}$ (22.2 GHz) transitions. The intensity is given in units of antenna temperature T_A^* (K), and the abscissa is $V_{\rm LSR}$ (km s^{-1}). The red dotted line represents the stellar velocity of 5.3 km s^{-1} (Chapman & Cohen 1986). (An extended version of this figure is available.)

4.3. Peak Antenna Temperature Ratios of H_2O and SiO Maser Lines

Figure 7(a) displays the peak antenna temperature ratios of the SiO masers to the H_2O maser. The intensity ratios between H_2O and SiO masers are associated with different evolutionary stages of host stars, as well as changing physical conditions according to pulsation phases on the same stars (Kim et al. 2014). Kim et al. (2014) reported the average values of the

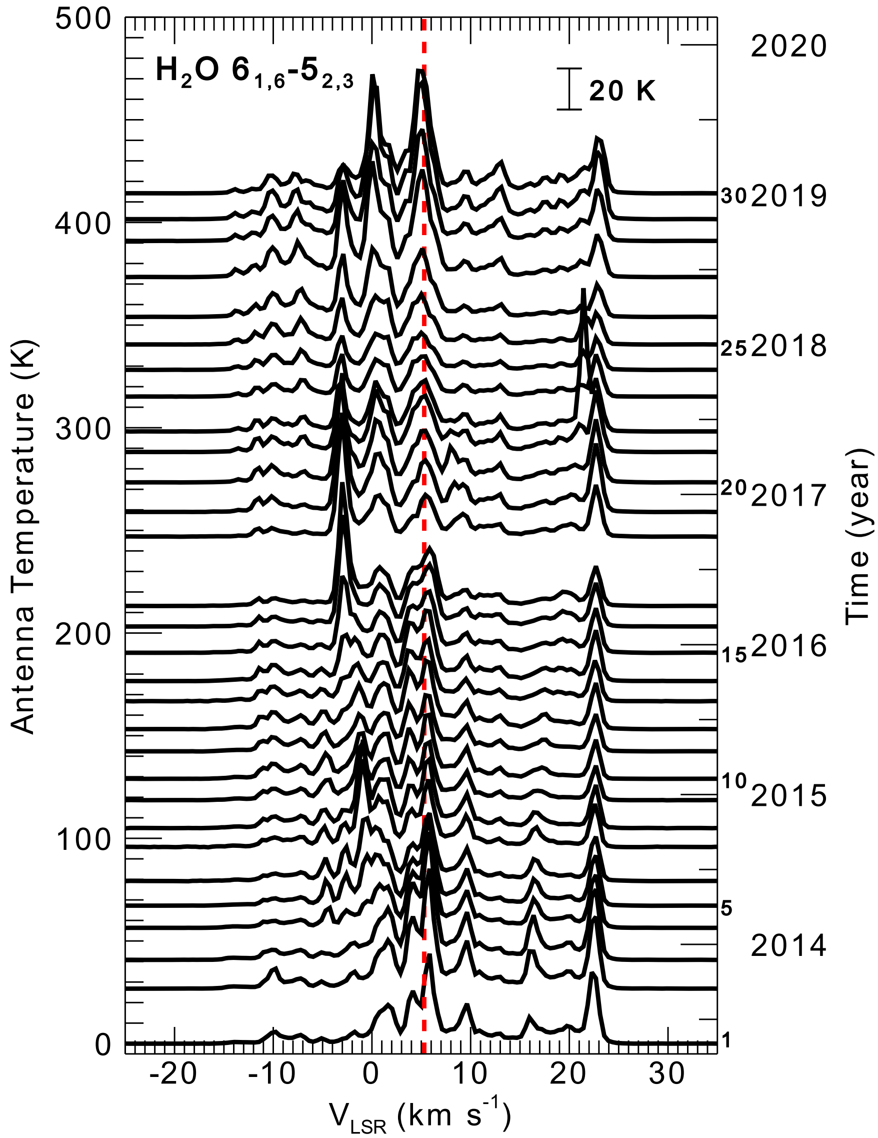

Figure 3. Variations of the H_2O $6_{1,6}$–$5_{2,3}$ maser spectra according to observation epochs. The red dotted line in the middle represents the stellar velocity of 5.3 km s^{-1}. The *y*-axis is the antenna temperature, and the spectra are arranged according to observational dates (epochs). The observational dates and epochs are marked on the right side of the vertical axis.

peak and integrated antenna temperature ratios of SiO and H_2O masers in the evolutionary stages of Mira variables and OH/IR stars. According to their statistical maser studies, the average peak and integrated intensity ratios of the 43.1 GHz SiO maser to 22.2 GHz H_2O are 0.64 and 0.92 for OH/IR stars and 0.72 and 1.43 for Mira variables, respectively. Additionally, the peak and integrated antenna temperature ratios are 0.31 and 0.99 for semiregular variables, respectively (Kim et al. 2013). As shown in Figure 7(a), the peak antenna temperature ratios of the 43.1 GHz SiO maser to 22.2 GHz H_2O in VX Sgr are 0.07–0.68, depending on the phase, and the average value is 0.28. The average value is the total value of the ratio divided by the number of epochs observed. Since these ratios change according to pulsation phases, we took the average ratio as a representative value of the peak antenna temperature ratios.

These values are smaller than those of OH/IR stars and Mira variables and similar to the average value of semiregular variables (Kim et al. 2013). In other words, the intensities of the H_2O maser from VX Sgr are much stronger than those of the SiO maser in OH/IR stars and Mira variables. Object VX Sgr may spout a stronger outflow from the central star, as its mass is higher than that of OH/IR and Mira. The active H_2O maser is probably generated from the high density of H_2O molecules and shocks due to high mass loss. The SiO maser is generated near the central star inside a dust layer (∼2–4 R_*; Diamond et al. 1994), but the 22.2 GHz H_2O maser is generated in the outer region that is about 10 times of the SiO maser region above the dust layer.

However, statistical studies have suggested that the influence of radiation on these masers is almost simultaneous (Kim et al. 2014). The intensity ratio of the H_2O and SiO masers according to the optical phase will exhibit a difference between the SiO and H_2O maser reactions because SiO masers are pumped by both radiation and collision, but H_2O masers are mainly

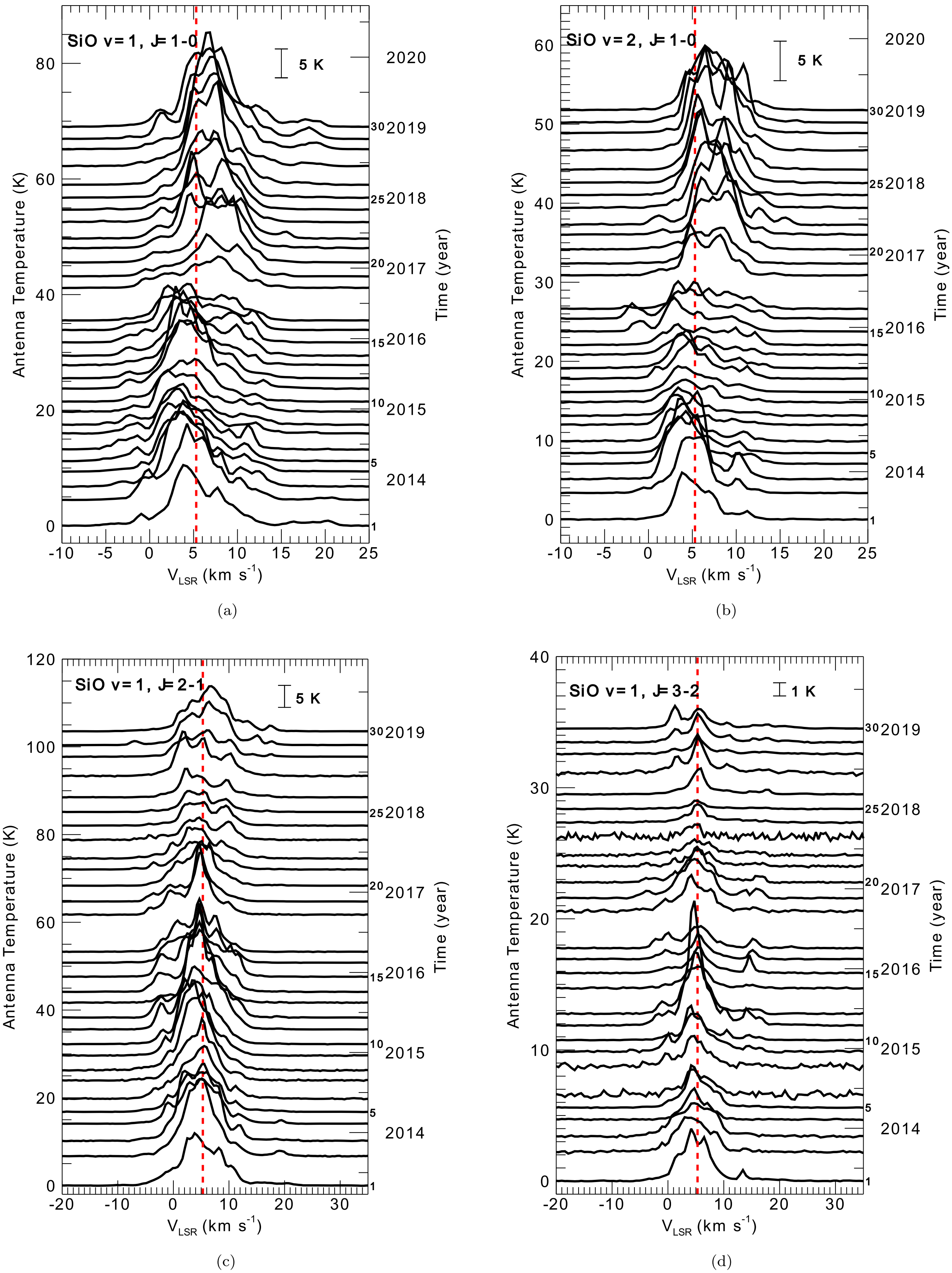

Figure 4. Variations of the SiO $v = 1, 2$, $J = 1–0$; $v = 1$, $J = 2–1$, $J = 3–2$ (43.1, 42.8, 86.2, 129.3 GHz) maser spectra according to the observational epochs. The red dotted line in the middle represents the stellar velocity of 5.3 km s^{-1}. Other indices are the same as in Figure 3.

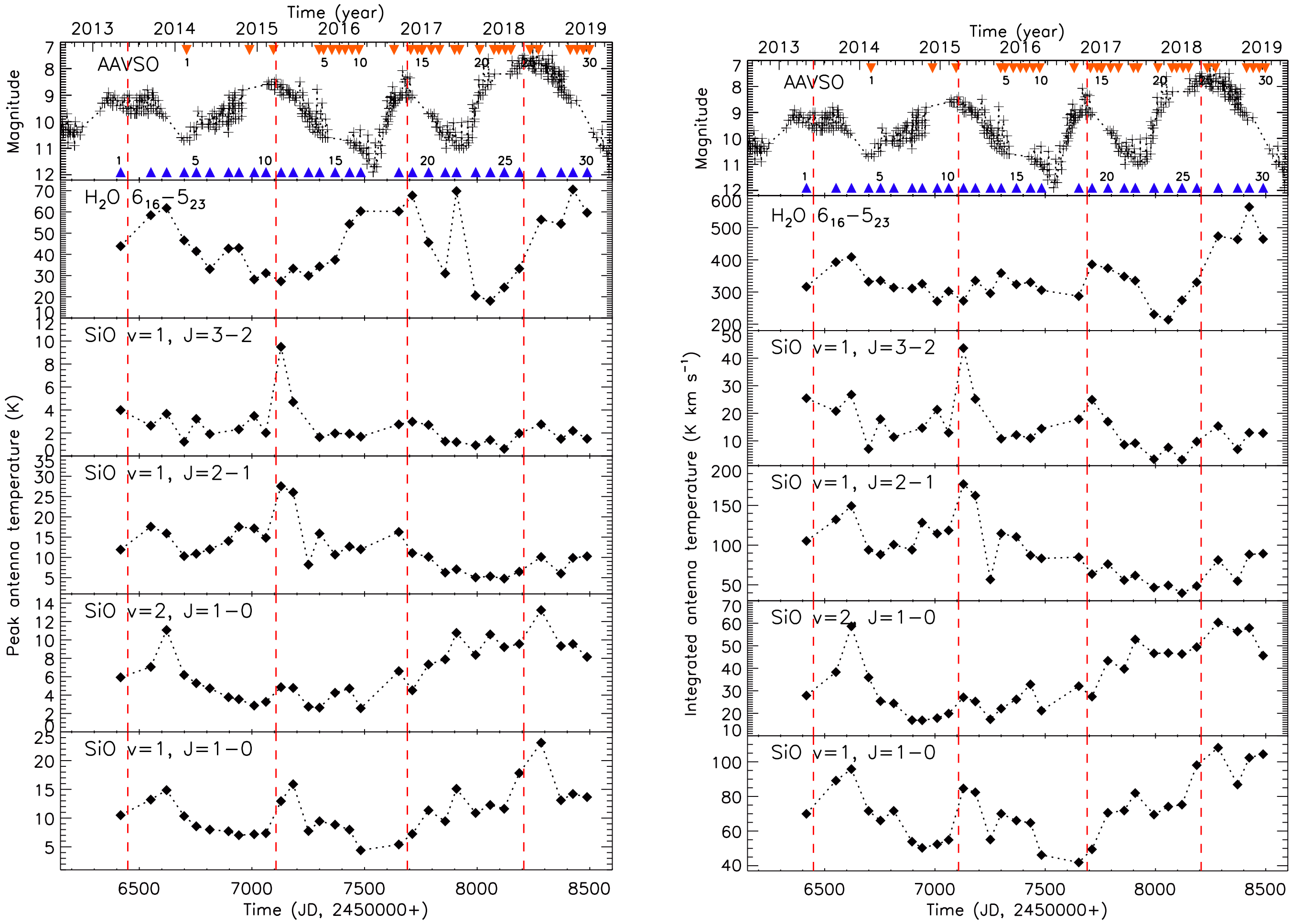

(a) Peak antenna temperature

(b) Integrated antenna temperature

Figure 5. Peak and integrated antenna temperature variations of the H_2O and SiO masers according to observational dates (Julian dates). The first row is the optical magnitude variation of VX Sgr from the AAVSO. Blue and red triangles correspond to the single-dish and VLBI observations, respectively. The red dashed lines indicate the optical brightness maxima according to the optical phases.

pumped by collision. The peak intensity ratios of the SiO masers (43.1, 42.8, 86.2, and 129.3 GHz) to the H_2O maser show a maximum around the second optical maximum (Figure 7(a)). However, the tendency is different around the fourth optical maximum. The peak intensity ratio of SiO to H_2O exhibits the maxima before the fourth optical maximum for the 43.1, 42.8, and 86.2 GHz SiO masers. On the other hand, the ratio of the 129.3 GHz SiO masers to the H_2O maser exhibits a maximum near the fourth optical maximum. The maximum ratios around the second optical maximum appear to be caused by the missing maximum of the H_2O maser around these optical maxima, and each maximum of the SiO masers seems to be reflected. The peak intensity ratios of the 86.2 GHz SiO maser to the H_2O maser exhibit the highest value of about 1.01 around the second optical maximum.

Figure 7(b) displays the peak antenna temperature ratios of the H_2O maser and 42.8, 86.2, and 129.3 GHz SiO masers with respect to the 43.1 GHz SiO maser. The intensity ratio of the 42.8 GHz SiO maser to the 43.1 GHz SiO maser varies from 0.28 to 1.22 according to the phase, and its average value is 0.60. This ratio around the third optical maximum (2016 September) reaches approximately ∼1.2. Yoon et al. (2014) suggested that the 42.8 GHz SiO maser tends to be stronger than the 43.1 GHz, and the average ratio of the 42.8 GHz to the 43.1 GHz SiO maser is 2.83 in post-AGB stars due to the development of hot dust layers. For OH/IR stars, these ratios are 0.89 (Cho et al. 2017), 0.98 (Cho & Kim 2012), and 0.83 (Kim et al. 2013) in the survey observations. These ratios for Mira and semiregular variables are 0.90 and 0.87, respectively (Kim et al. 2013). Supergiants have an average ratio of 0.61 (Kim et al. 2010) for six stars, which is comparable to the ratio of VX Sgr. The intensity ratios of the 86.2 GHz to the 43.1 GHz SiO maser vary from 0.36 to 3.01, and the average value is 1.29. The intensity ratios of the 129.3 GHz to the 43.1 GHz SiO maser vary from 0.05 to 0.73, and the average value is 0.25 according to the phase. In the statistical studies of masers, the intensity ratio of each SiO transition line varies according to the evolutionary stage (Kim et al. 2013, 2014). Also, the stellar pulsation phase is an important factor in determining the intensity ratio of each transition line.

4.4. Full Width at Zero Power Variations of H_2O and SiO Masers

Half of the full width at zero power (FWZP) value gives the expansion velocity information in maser-emitting regions.

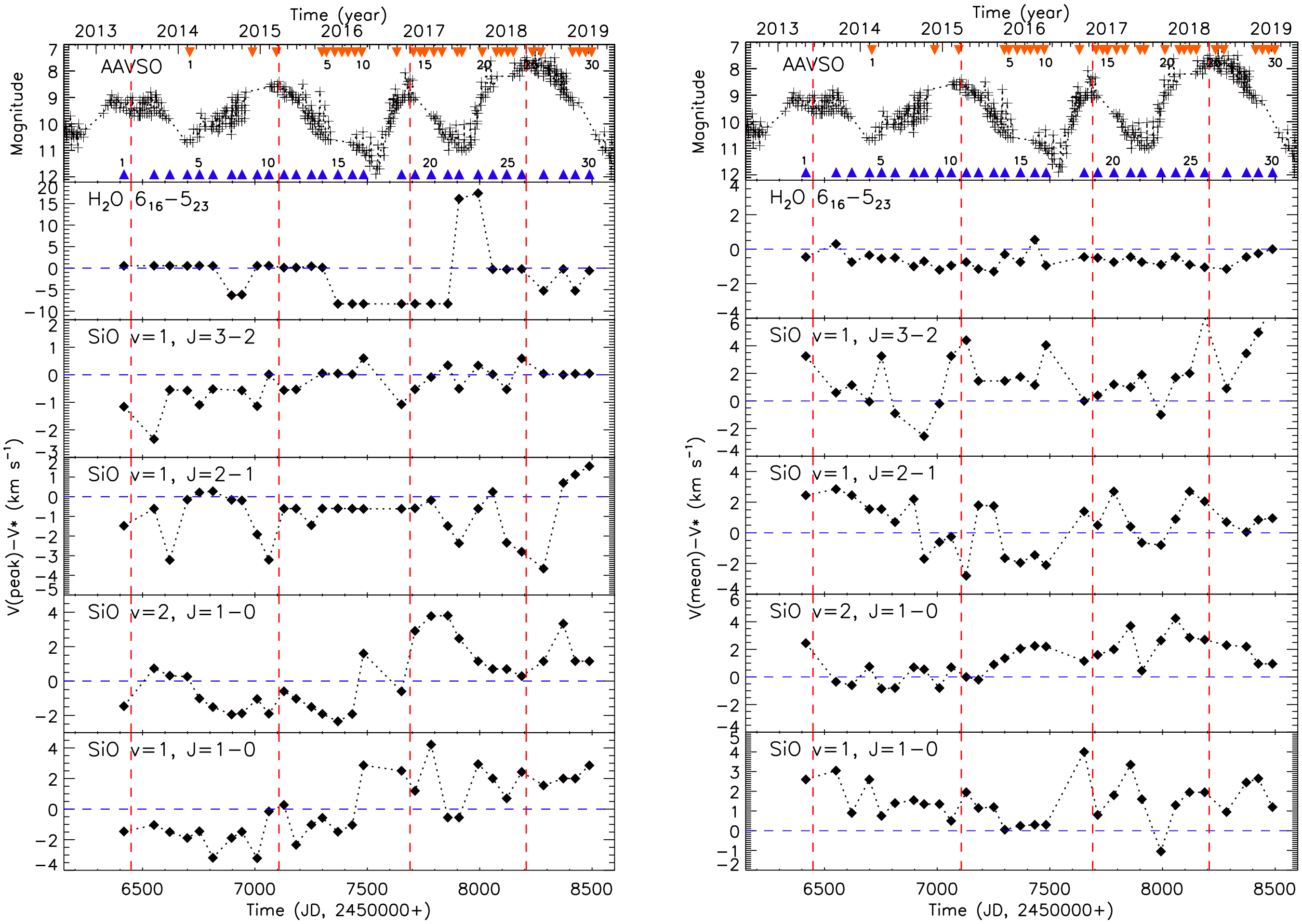

(a) Peak velocity variation

(b) Mean velocity variation

Figure 6. Peak and mean velocity variations of each maser spectrum according to the observational dates. The reference of the blue dotted line on the abscissa is the stellar velocity V_* of VX Sgr ($V_* = 5.3$ km s^{-1}). The other indices are the same as in Figure 5.

Figure 8 shows variations of FWZP values according to the date. The FWZPs were measured at both ends (blue and red edge) of each maser line above the 1σ noise level based on the Gaussian fitting baseline (Table 2). The H_2O masers have an FWZP of 39.2–49.1 km s^{-1} (average FWZP: 41.6 km s^{-1}) above the rms noise level of 0.015–0.079 K. The largest FWZP of 49.1 km s^{-1} was observed on 2018 June 15, as shown in Figures 8 and 9, ranging from −19.9 to 29.2 km s^{-1}. The average expansion velocity of the H_2O maser derived from the average FWZP was about 20.8 ± 0.9 km s^{-1}. The expansion velocity measured by the CO $J = 2$–1 line (i.e., terminal velocity) was 26 km s^{-1}, ranging from −19 to 33 km s^{-1} (Gonzalez-Alfonso et al. 1998). Therefore, the expansion velocity in the H_2O maser region has not yet reached the terminal velocity. Determining the correlation between the FWZPs and the optical phases is difficult in both H_2O and SiO masers.

Furthermore, SiO masers exhibit FWZPs of 20.0–29.6 km s^{-1} (average FWZP: 25.0 km s^{-1}) for the 43.1 GHz maser, 15.8–27.6 km s^{-1} (average FWZP: 20.4 km s^{-1}) for the 42.8 GHz maser, 22.2–36.5 km s^{-1} (average FWZP: 27.8 km s^{-1}) for the 86.2 GHz maser, and 2.6–34.2 km s^{-1} (average FWZP: 21.9 km s^{-1}) for the 129.3 GHz maser above the rms noise level of 0.014–0.169 K (Table 2). The FWZPs of the H_2O maser are always larger than those of the SiO masers. Additionally, FWZP's blue- and red-edge velocities with respect to the stellar velocity of each maser line are presented in Figure 9. Figure 9 shows the variations of H_2O and four SiO maser lines at once, and the blue-edge velocity with respect to stellar velocity gives an approaching expansion velocity, while the red-edge velocity gives a receding velocity. The variations of the blue- and red-edge velocities of the H_2O maser are more stable than those of the SiO masers. This is because of the different formation regions of the two masers. The SiO masers are generated inside the dust layer, which is affected by the outward and infall motions associated with stellar pulsation. The 42.8 GHz SiO maser is located at the innermost region, followed by the 43.1, 86.2, and 129.3 GHz masers (Yoon et al. 2018). In contrast, the H_2O maser is generated outside the dust layer, which is affected by the accelerating motion due to the radiation pressure on the dust.

In single-dish observations, the spectra are obtained by combining all velocity components with a large single beam. Even if a particular maser feature represents the local velocity, the single-dish results can represent the velocity dispersion of the entire velocity field because it detects all of the combined velocity components without exception. The emitting regions of SiO masers are accelerated, and the acceleration decreases as

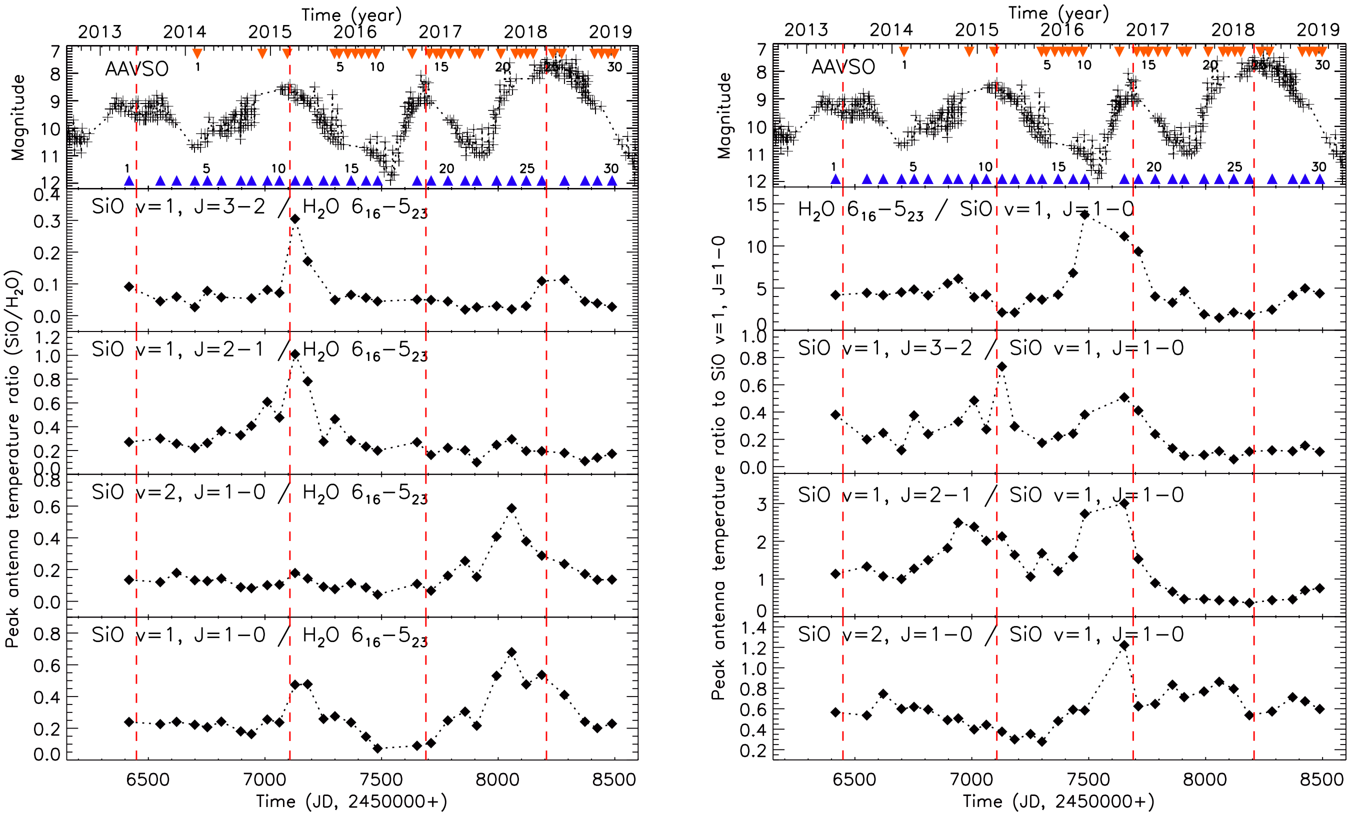

(a) SiO / H_2O maser (b) Other SiO and H_2O / 43.1 GHz SiO maser

Figure 7. Peak antenna temperature ratios of the H_2O and SiO masers according to the observational dates. The other indices are the same as those in Figure 5.

distance increases, although the motion inside the dust layer is complicated (Yun & Park 2012). The velocity dispersion of the maser lines of the 42.8 GHz SiO maser could be smaller than that of other SiO masers, since it is located in the large velocity gradient region close to the central star, which could yield a small FWZP. In Table 2, the FWZP of the 43.1 GHz SiO maser is larger than that of the 42.8 GHz SiO maser by up to 15 km s^{-1} in most cases, except in three epochs. The difference in the FWZPs is up to 25 km s^{-1} for the 86.2 GHz SiO maser, which is located more outside regions than the 42.8 and 43.1 GHz masers. On the other hand, the difference between the averaged FWZP values of the 42.8 and 129.3 GHz SiO masers is not large compared to the other transition. Yoon et al. (2018) reported that the generated region of the 129.3 GHz SiO maser varies according to optical phases and is about 20% further away than that of the 43.1 GHz SiO maser. The relatively small FWZP of the 129.3 GHz maser compared to its outermost generated region is likely due to a low noise level. When the 129.3 GHz SiO maser exhibits the strongest intensity (9.49 K) around the second optical maximum (11th epoch; Figure 5), its FWZP (34.2 km s^{-1}) is larger than that of the 43.1 GHz maser (24.3 km s^{-1}) and comparable to that of the 86.2 GHz maser (34.8 km s^{-1}).

5. Discussion

5.1. Possibility of Acceleration and Development of Asymmetry from SiO Maser Regions to the H_2O Maser Region

The 22.2 GHz H_2O maser generated by collisional pumping illustrates the kinematics of the H_2O maser region in the circumstellar envelope. It requires a lower temperature and density compared to the SiO masers. The H_2O maser stems from above dust layers in evolved stars, where the expansion velocity is still accelerating and the terminal velocity has not been reached. We discuss how these expansion velocities can be accelerated from the SiO maser region through the dust layer to 20.8 ± 0.9 km s^{-1} in the H_2O maser region and also from the expansion velocity of the H_2O maser region to the terminal velocity of 26 km s^{-1} measured by the CO $J = 2$–1 line.

We investigate the possibility of the acceleration by analyzing the H_2O maser monitoring observations. The complex line profiles of the H_2O maser that are present in the single-dish observations are the combined features of the various components. Figure 10 shows the H_2O maser spectrum with an enlarged lower part on 2016 February 15 ($\phi = 1.56$). We denote 11 components from (a) to (k) in the line profile. Figure 11 shows the behaviors of these 11 components that survive during the monitoring observations and are traceable. Table 3 provides the peak antenna temperatures and velocities of the H_2O maser components from (a) to (k). A single peak in the individual component represents the strongest maser component within the related velocity range in our spectral resolution. The peak velocity variations of the 11 components over time can be classified into three patterns. In the first pattern, the peak velocity barely changes over time within our velocity resolution during the monitoring observations (e.g., lower panels of (i) and (k) in Figure 11). In the second pattern, the peak velocity increases and decreases with time (e.g., in panels (b) and (h) in Figure 11, the peak velocity decreases around the optical maxima). In the third pattern, the peak

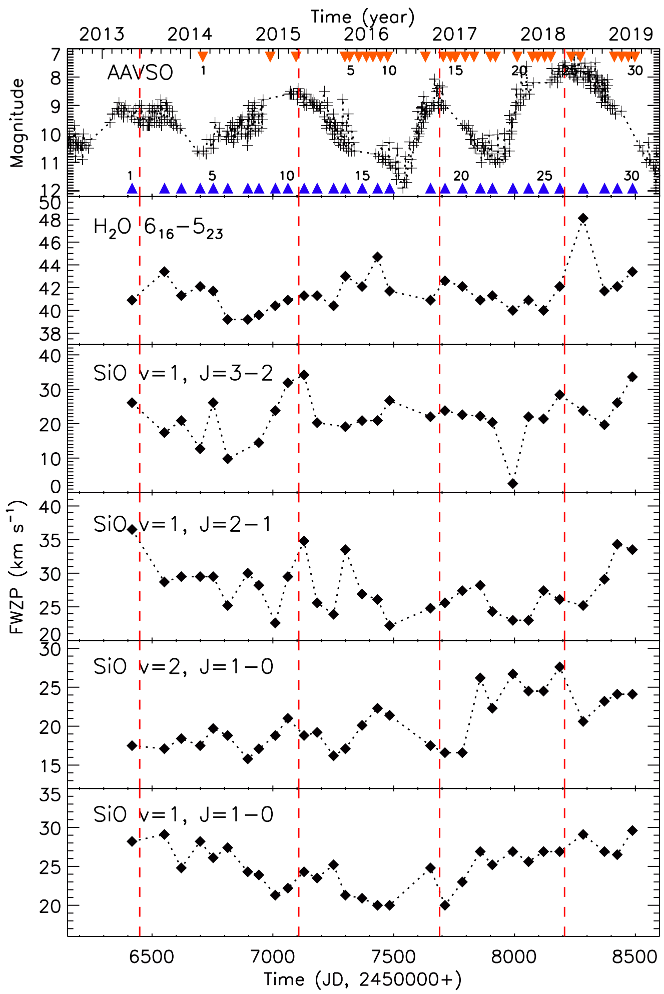

FWZP of each maser transition

Figure 8. The FWZPs according to the observational dates. The other indices are the same as in Figure 5.

velocity gradually decreases or increases during the monitoring observations (e.g., decrease: panels (a), (c), (d), (e), (f), and (g); increase: panel (j) in Figure 11). For the first pattern, the peak velocity of the strongest component is presumed to not change within the specific velocity range during our observations. For example, the K component of the H_2O maser moves away with respect to the central star with a constant velocity of ∼17.4 km s^{-1}. In the second pattern, the peak velocity of the strongest maser component in the B component is assumed to vary from –15.0 to –15.4 km s^{-1} during our observations. This pattern is expected to be a mixture of several components in a similar velocity range, which our single-dish resolution cannot distinguish. The repetition of similar velocity components is possibly due to the different dominance of each unresolved independent component within the limited velocity range, depending on the epochs. We assume that the components of the same velocity that are present on the red dotted lines are probably similar velocity components (Figures 11(b) and (h)). In the third pattern, the increasing and decreasing peak velocities denote that the maser is accelerating along the line of sight.

We focus on the third pattern that signifies acceleration. In Figure 11, the six ((a), (c), (d), (e), (f), and (g)) components indicate decreasing peak velocity (blueshifted with respect to the central star), and only the (j) component denotes increasing peak velocity (redshifted). In particular, the peak velocities of the (e) and (j) components significantly change; i.e., they are accelerated in a certain epoch compared to the other components but remain constant thereafter. We derive the acceleration of the (e) and (j) components using the velocity change over a specific period ((e) is the 6th–15th epochs, and (j) is the 1st–11th epochs). The calculated acceleration in the line of sight of components (e) and (j) is −1.67 and 0.87 km s^{-1} yr^{-1} from the velocity change, respectively. The time taken to accelerate from 20.8 km s^{-1} in the H_2O maser region to the terminal velocity of 26 km s^{-1} is 3.1 and 6.0 yr, respectively.

On the other hand, the peak velocities of the (a) and (d) components are gradually blueshifted with respect to the central star over time. The corresponding acceleration of the (a) and (d) components is −0.28 and −0.44 km s^{-1} yr^{-1}, respectively. Moreover, the acceleration is dominant in the blueshifted components compared to the redshifted components, and the acceleration rates differ based on the components of the H_2O maser lines. These kinds of different behaviors of H_2O maser lines may cause more asymmetry.

The possibility of H_2O maser acceleration and asymmetry was investigated through the analysis of the peak velocity variations of each component in the line profile according to the date. Furthermore, the kinematics of the H_2O maser region is associated with the atmospheric dynamics of the SiO maser formation regions located between the stellar surface and the dust layers. Yoon et al. (2018) argued that the local radial acceleration of the SiO maser formation regions exerts a different radiation pressure on the dust layers, leading to asymmetry of the H_2O maser formation region. They suggested that the regional kinematics difference of the velocity components will lead to the inhomogeneity and asymmetry of the H_2O maser spatial distribution.

Figure 11 examines the relation among the peak intensities of each component in the single-dish line profile of the H_2O maser and pulsation phases. In the lower right corner of Figure 11, the optical magnitude variations of VX Sgr from AAVSO and the corresponding maxima are shown with blue dashed–dotted lines. Analysis of the peak intensity of each component gives more detailed information than the entire spectrum. In Figure 5(a), the peak antenna temperature of the H_2O maser does not exhibit the intensity maximum around the second optical maximum, unlike the first, third, and fourth maxima. However, the (a), (b), (c), and (k) components exhibit intensity maxima around or after the second optical maxima in Figure 11. Additionally, the (g), (i), and (j) components exhibit the weak maxima of their intensities after the second optical maximum.

To compare the single-dish spectrum of the H_2O maser with the VLBI results, the KVN VLBI monitoring results of 2016 January 26 ($\phi = 1.53$) are provided in Figure 12, which is the closest to the single-dish observation date of 2016 February 15 ($\phi = 1.56$). Figure 12(a) displays the moment zero map of VLBI observation, (b) displays a position–velocity spot map of VLBI observation, and (c) displays the recovered flux in VLBI observation superposed on the single-dish spectrum of 2016 February 15. The position of the central star is set to (0.0) in Figures 12(a) and (b), which

Table 2
FWZPs of H_2O and SiO Maser Lines

Date (yymmdd)	H_2O			SiO											
	$6_{1,6}-5_{2,3}$			$v=1$, $J=1$–0			$v=2$, $J=1$–0			$v=1$, $J=2$–1			$v=1$, $J=3$–2		
	Blue Edge	Red Edge	FWZP (km s^{-1})	Blue Edge	Red Edge	FWZP (km s^{-1})	Blue Edge	Red Edge	FWZP (km s^{-1})	Blue Edge	Red Edge	FWZP (km s^{-1})	Blue Edge	Red Edge	FWZP (km s^{-1})
(1)	(2)	(3)	(4)	(5)	(6)	(7)	(8)	(9)	(10)	(11)	(12)	(13)	(14)	(15)	(16)
130505	−15.6	25.2	40.9	−6.2	22.1	28.2	−1.0	16.5	17.5	−10.5	26.0	36.5	−4.5	21.5	26.1
130916	−16.1	27.3	43.4	−6.2	22.9	29.1	−3.6	13.4	17.1	−6.2	22.5	28.7	−2.8	14.6	17.4
131125	−16.1	25.2	41.3	−6.2	18.6	24.8	−4.5	13.9	18.4	−7.0	22.5	29.5	−4.0	16.9	20.9
140211	−16.1	26.1	42.1	−6.2	22.1	28.2	−2.7	14.8	17.5	−7.9	21.6	29.5	−1.1	11.7	12.7
140406	−16.1	25.6	41.7	−7.0	19.0	26.1	−5.4	14.3	19.7	−7.9	21.6	29.5	−4.5	21.5	26.1
140605	−14.8	24.4	39.2	−7.0	20.3	27.4	−4.9	13.9	18.8	−6.6	18.6	25.2	−0.5	9.4	9.8
140827	−15.3	23.9	39.2	−5.3	19.0	24.3	−1.9	13.9	15.8	−7.5	22.5	30.0			
141012	−15.2	24.4	39.6	−5.3	18.6	23.9	−2.7	14.3	17.1	−10.5	17.7	28.2	−4.5	10.0	14.5
141219	−16.1	24.4	40.4	−4.0	17.3	21.3	−4.9	13.9	18.8	−6.6	16.0	22.6	−6.8	16.9	23.8
150209	−16.1	24.8	40.9	−5.3	16.9	22.2	−4.5	16.5	21.0	−9.7	19.9	29.5	−7.4	24.4	31.9
150417	−16.1	25.2	41.3	−4.9	19.5	24.3	−4.1	14.8	18.8	−14.9	19.9	34.8	−7.4	26.8	34.2
150610	−16.5	24.8	41.3	−5.3	18.2	23.5	−4.5	14.8	19.2	−5.7	19.9	25.6	−3.4	16.9	20.3
150817	−16.2	24.3	40.4	−6.1	19.0	25.2	−1.9	14.3	16.2	−4.9	19.0	23.9			
151005	−16.5	26.5	43.0	−5.3	16.0	21.3	−1.9	15.2	17.1	−13.1	20.3	33.5	−2.8	16.3	19.1
151213	−16.5	25.6	42.1	−4.9	16.0	20.9	−2.7	17.4	20.1	−10.1	16.9	26.9	−3.4	17.5	20.9
160215	−16.5	28.2	44.7	−4.4	15.6	20.0	−3.6	18.7	22.3	−9.2	16.9	26.1	−4.0	16.9	20.9
160405	−16.5	25.2	41.7	−4.4	15.6	20.0	−3.2	18.3	21.4	−7.9	14.2	22.2	−4.0	22.7	26.7
160921	−15.6	25.2	40.9	−3.1	21.7	24.8	−2.3	15.2	17.5	−5.7	19.0	24.8	−5.7	16.4	22.0
161120	−16.5	26.1	42.6	−3.9	16.0	20.0	−1.4	15.2	16.6	−7.0	18.6	25.6	−6.2	17.5	23.8
170131	−16.5	25.6	42.1	−4.4	18.6	23.0	−1.0	15.6	16.6	−5.7	21.6	27.4	−4.8	17.8	22.6
170415	−15.6	25.2	40.9	−4.8	22.1	26.9	−4.1	22.2	26.2	−8.4	19.9	28.2	−4.8	17.4	22.2
170604	−16.1	25.2	41.3	−5.7	19.5	25.2	−5.4	16.9	22.3	−7.5	16.9	24.3	−3.0	17.4	20.4
170828	−15.6	24.4	40.0	−9.2	17.8	26.9	−5.4	21.3	26.7	−7.0	16.0	23.0	3.0	5.6	2.6
171101	−15.6	25.2	40.9	−6.2	19.5	25.6	−2.7	21.8	24.5	−5.3	17.7	23.0	−4.0	18.1	22.0
180102	−15.6	24.4	40.0	−6.2	20.8	26.9	−4.1	20.4	24.5	−5.7	21.6	27.4	−3.4	18.1	21.4
180310	−16.8	25.3	42.1	−6.2	20.8	26.9	−5.8	21.8	27.6	−5.7	20.3	26.1	−2.8	25.6	28.4
180615	−19.9	29.2	49.1	−8.3	20.8	29.1	−2.7	17.8	20.6	−6.6	18.6	25.2	−5.7	18.1	23.8
180910	−16.0	25.8	41.7	−5.7	21.2	26.9	−4.1	19.1	23.2	−9.2	19.9	29.1	−1.1	18.6	19.7
181103	−16.0	26.2	42.1	−5.3	21.2	26.5	−5.8	18.3	24.1	−11.0	23.4	34.3	−2.8	23.3	26.1
190105	−16.4	27.0	43.4	−8.3	21.2	29.6	−5.8	18.3	24.1	−10.5	22.9	33.5	−4.5	29.1	33.6

was determined through previous SiO maser VLBI observations (Yoon et al. 2018). The moment zero map (panel (a)) shows the integrated intensity distribution over the maser spectral line. On the other hand, the position–velocity spot map (panel (b)) includes the velocity information of maser spots. The total intensity of VLBI is less than that of single-dish observations due to a sharp beam size and incompletely filled UV plane within KVN (Yoon et al. 2014). Therefore, analysis of the peak velocity of each component based on single-dish observations can more accurately depict the characteristics of the maser spots in the components within the velocity range compared to the VLBI observations.

The H_2O maser spots are spread out and widely distributed with various velocity components in the VLBI results, as shown in Figure 12(b). Each component of the single-dish spectrum in Figure 10 represents the sum of the maser spots covering each velocity range in the VLBI image, and the components appear as a peak at the velocity of the strongest maser spot. Recovered flux from the VLBI observation (Figure 12(c)) shows prominent peaks around −3 and 23 km s^{-1}, and most of the flux is distributed around −3 km s^{-1}. Also, the strongest flux around –3 km s^{-1} is mainly located in the red dotted square (Figures 12(a) and (b)), which corresponds to the (d)–(f) components in the single-dish spectrum (Figure 11). The velocity range of the (d)–(f) components in Figure 11 is from −6 to 3 km s^{-1}.

We quantitatively compared the number and intensity of the (d)–(f) maser spots in the VLBI map. In Figure 12(a), of all the spots in the range of −6 to 3 km s^{-1}, the proportion of maser spots located in the red dotted square to the total number is 59.0% (23 inside, 39 total), while the intensity percentage is 88% (1351 Jy beam^{-1} km s^{-1} inside, 1529 Jy beam^{-1} km s^{-1} total). Most of the strong flux part that can be distinguished by VLBI is located to the southeast of the stellar position. Despite the optically minimum period, the (e) component tends to be rather strong, showing a different pattern from other components. At this time, the peak antenna temperature increases, but the integrated antenna temperature changes little, as shown in Figure 5. We speculate that encouragement of the H_2O maser generation is occurring in the red dotted square region corresponding to the (e) component. The interaction between the outflow and surrounding materials near the red dotted square may be a dominant factor for the strongest maser pumping of the H_2O maser.

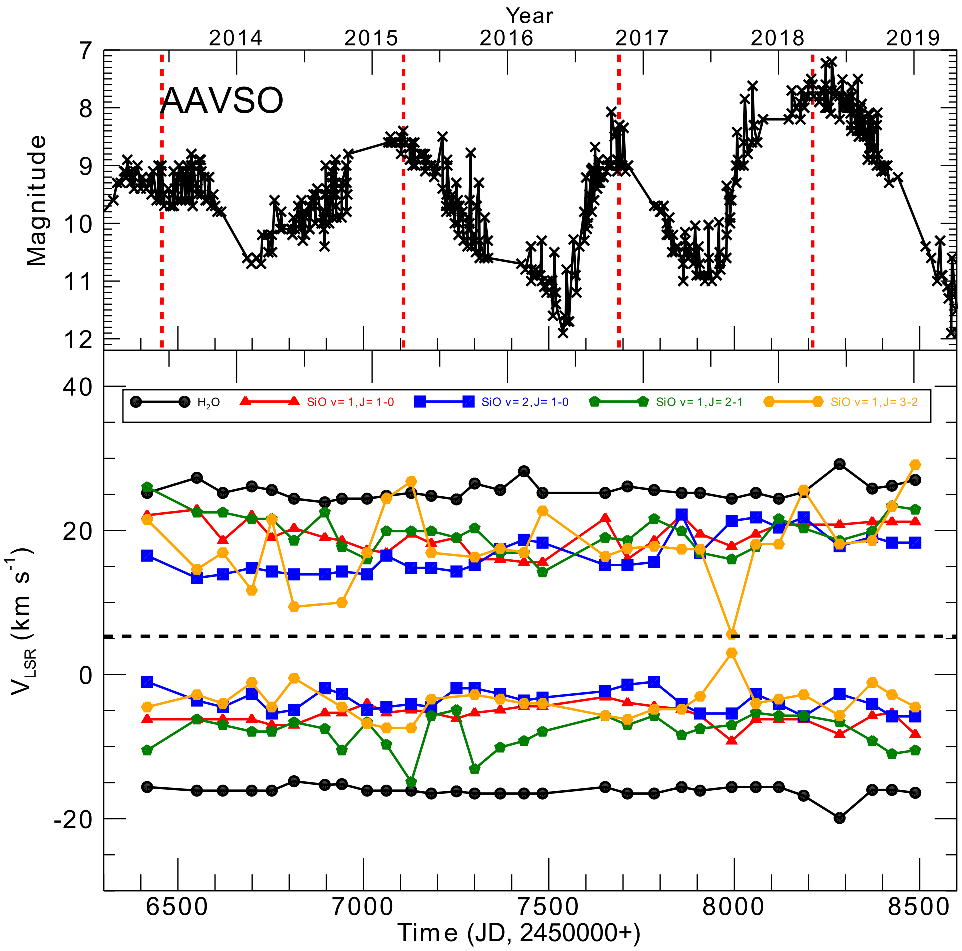

Figure 9. Blue- and red-edge velocity variations of each maser line with respect to the stellar velocity. As indicated in the upper box, the black circles, red triangles, blue squares, green pentagons, and yellow hexagons indicate the H_2O (22.2 GHz) and SiO (43.1, 42.8, 86.2, and 129.3 GHz) masers, respectively. The black dotted line on the horizontal axis represents the stellar velocity, which demarcates the blue- and redshifted spectral boundaries. The *x*- and *y*-axes represent the modified Julian date and local standard of rest (LSR) velocity, respectively.

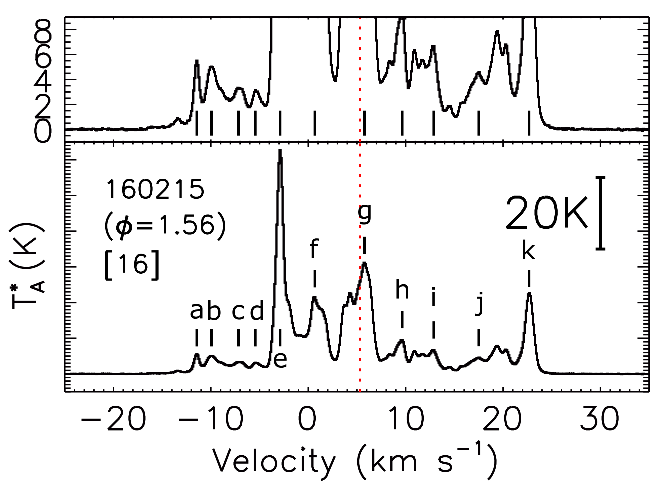

Figure 10. The H_2O maser spectrum on 2016 February 15 ($\phi = 1.56$) obtained with the KVN single-dish telescope. The upper panel indicates the enlarged vertical axis, displaying a weak spectrum. In the lower panel, the short black lines represent the positions of spectra from (a) to (k). The vertical red dotted line indicates the stellar velocity ($V_* = 5.3$ km s^{-1}).

5.2. Characteristics of Four SiO Maser Lines

The intensity and velocity variation trend of the 43.1 GHz SiO maser was similar to that of the 42.8 GHz SiO maser rather than the 86.2 and 129.3 GHz SiO masers in Figures 5 and 6. The similarity was also found between the 86.2 and 129.3 GHz SiO masers. In Figure 6, the peak velocities of the 43.1 and 42.8 GHz SiO masers were dominated by blueshift until 2016 April and by redshift thereafter (Figure 6(a)). On the other hand, the peak velocities of the 86.2 and 129.3 GHz SiO masers were dominated by blueshift during most of the monitoring period. The peak velocity variations of the 129.3 GHz SiO maser occurred around the stellar velocity compared to those of the 86.2 GHz SiO. These characteristics show that the 43.1 and 42.8 GHz SiO maser properties are different from the 86.2 and 129.3 GHz SiO maser properties as reported in the long-term KVN single-dish monitoring observations toward V627 Cas (Yang et al. 2020).

The different characteristics among the four transition SiO masers may stem from the different locations of each maser, which reflect different excitation conditions. Yoon et al. (2018)

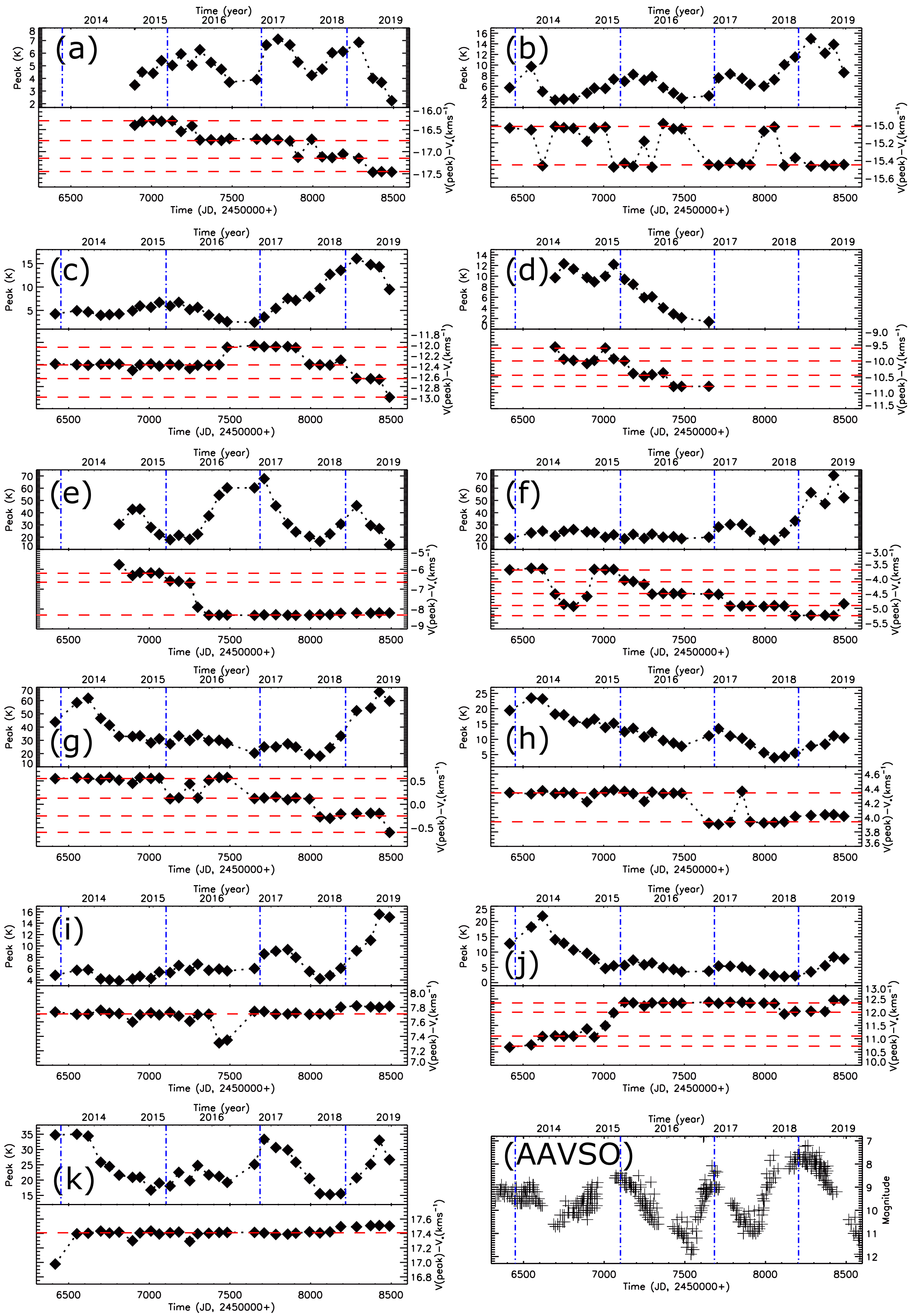

Figure 11. Velocity and intensity variations of the H_2O maser components from (a) to (k) over time. The upper and lower panels represent the peak antenna temperature and velocity difference of each component with respect to the stellar velocity ($V_* = 5.3$ km s^{-1}), respectively. The horizontal red dotted line represents a set of similar peak velocities within our velocity resolution. The lower right panel displays the magnitude variation in AAVSO.

Table 3
Peak Antenna Temperature and Velocity of H_2O Maser Components

Date (yymmdd) (1)	a T_A^* (peak) (K) (2)	a velocity (km s^{-1}) (3)	b T_A^* (peak) (K) (4)	b velocity (km s^{-1}) (5)	c T_A^* (peak) (K) (6)	c velocity (km s^{-1}) (7)	d T_A^* (peak) (K) (8)	d velocity (km s^{-1}) (9)
130505	⋯	⋯	5.73	−9.73	4.26	−7.19	⋯	⋯
130916	⋯	⋯	9.72	−9.75	4.94	−7.20	⋯	⋯
131125	⋯	⋯	4.99	−10.16	4.68	−7.22	⋯	⋯
140211	⋯	⋯	3.39	−9.72	3.96	−7.19	9.69	−4.26
140406	⋯	⋯	3.54	−9.73	4.09	−7.19	12.33	−4.65
140605	⋯	⋯	3.65	−9.74	4.26	−7.19	11.33	−4.68
140827	3.48	−11.10	4.69	−9.88	4.90	−7.33	9.73	−4.78
141012	4.51	−11.02	5.66	−9.73	5.95	−7.21	8.92	−4.68
141219	4.41	−10.99	5.58	−9.72	5.67	−7.19	9.99	−4.29
150209	5.41	−11.01	7.33	−10.17	6.73	−7.24	12.21	−4.63
150417	5.03	−11.01	6.94	−10.13	5.94	−7.20	9.39	−4.70
150610	5.94	−11.24	8.23	−10.17	6.72	−7.21	8.45	−5.10
150817	5.04	−11.12	7.15	−9.88	5.19	−7.29	5.95	−5.18
151005	6.27	−11.44	7.81	−10.18	5.65	−7.22	6.10	−5.13
151213	5.26	−11.43	5.76	−9.68	4.02	−7.22	4.02	−5.07
160215	4.72	−11.45	4.73	−9.74	3.25	−7.21	2.85	−5.50
160405	3.70	−11.41	3.75	−9.74	2.59	−6.81	2.15	−5.50
160921	3.91	−11.42	4.19	−10.15	2.46	−6.77	1.41	−5.50
161120	6.65	−11.42	7.58	−10.16	3.60	−6.80	⋯	⋯
170131	7.10	−11.43	8.32	−10.13	5.43	−6.80	⋯	⋯
170415	6.66	−11.46	7.49	−10.14	7.54	−6.79	⋯	⋯
170604	5.29	−11.83	6.36	−10.15	7.14	−6.82	⋯	⋯
170828	4.25	−11.42	6.02	−9.77	8.01	−7.20	⋯	⋯
171101	4.74	−11.82	7.24	−9.72	9.69	−7.21	⋯	⋯
180102	6.03	−11.84	10.06	−10.16	12.71	−7.22	⋯	⋯
180310	6.13	−11.75	11.51	−10.07	13.56	−7.10	⋯	⋯
180615	6.86	−11.85	14.95	−10.16	16.06	−7.52	⋯	⋯
180910	4.01	−12.16	12.23	−10.16	14.78	−7.52	⋯	⋯
181103	3.69	−12.15	13.89	−10.16	14.32	−7.54	⋯	⋯
190105	2.23	−12.16	8.59	−10.15	9.48	−7.94	⋯	⋯

Date (yymmdd) (1)	e T_A^* (peak) (K) (2)	e velocity (km s^{-1}) (3)	f T_A^* (peak) (K) (4)	f velocity (km s^{-1}) (5)	g T_A^* (peak) (K) (6)	g velocity (km s^{-1}) (7)	h T_A^* (peak) (K) (8)	h velocity (km s^{-1}) (9)
130505	⋯	⋯	18.93	1.61	43.86	5.85	19.43	9.64
130916	⋯	⋯	23.49	1.66	58.44	5.87	23.49	9.63
131125	⋯	⋯	24.95	1.64	61.77	5.85	23.20	9.67
140211	⋯	⋯	21.07	0.78	46.58	5.83	18.24	9.63
140406	⋯	⋯	24.85	0.43	41.45	5.87	18.00	9.65
140605	30.51	−0.47	26.20	0.37	33.05	5.82	15.87	9.63
140827	42.72	−1.01	24.38	0.70	32.91	5.75	15.28	9.52
141012	42.97	−0.87	23.73	1.62	33.48	5.87	16.60	9.63
141219	27.94	−0.88	19.97	1.61	28.17	5.85	13.88	9.66
150209	22.15	−0.90	21.98	1.62	31.14	5.86	15.23	9.68
150417	17.93	−1.29	18.66	1.25	27.29	5.42	12.48	9.66
150610	21.51	−1.31	22.29	1.21	33.28	5.44	13.59	9.63
150817	18.24	−1.40	18.99	1.12	29.93	5.74	10.81	9.52
151005	22.45	−2.61	22.51	0.78	34.26	5.43	12.23	9.65
151213	37.37	−3.01	20.01	0.81	29.78	5.81	9.62	9.63
160215	54.29	−3.01	20.39	0.80	30.04	5.87	8.76	9.64
160405	60.33	−3.01	18.75	0.80	27.86	5.87	7.74	9.64
160921	60.27	−3.02	19.94	0.78	20.34	5.42	11.13	9.22
161120	67.74	−2.99	28.35	0.78	25.07	5.44	13.44	9.21
170131	45.57	−2.99	30.34	0.38	25.08	5.46	11.07	9.23
170415	30.99	−3.01	30.32	0.38	27.37	5.40	10.34	9.66
170604	24.36	−3.02	24.59	0.38	24.91	5.44	8.35	9.24
170828	20.61	−3.00	18.09	0.36	19.56	5.41	5.65	9.22
171101	16.58	−2.98	17.56	0.39	18.07	5.03	3.96	9.23

Table 3
(Continued)

Date (yymmdd) (1)	e: T_A^* (peak) (K) (2)	e: velocity (km s^{-1}) (3)	f: T_A^* (peak) (K) (4)	f: velocity (km s^{-1}) (5)	g: T_A^* (peak) (K) (6)	g: velocity (km s^{-1}) (7)	h: T_A^* (peak) (K) (8)	h: velocity (km s^{-1}) (9)
180102	22.66	−2.97	23.59	0.38	24.39	5.00	4.46	9.24
180310	30.69	−2.91	33.30	0.05	33.24	5.09	5.46	9.31
180615	45.71	−2.90	56.38	0.06	52.32	5.10	7.83	9.33
180910	29.50	−2.91	47.37	0.06	54.40	5.11	8.40	9.34
181103	26.90	−2.89	70.52	0.05	66.59	5.10	11.10	9.34
190105	13.75	−2.90	52.26	0.45	59.62	4.70	10.46	9.32

Date (yymmdd) (1)	i: T_A^* (peak) (K) (2)	i: velocity (km s^{-1}) (3)	j: T_A^* (peak) (K) (4)	j: velocity (km s^{-1}) (5)	k: T_A^* (peak) (K) (6)	k: velocity (km s^{-1}) (7)
130505	4.83	13.04	12.78	15.98	34.76	22.28
130916	5.72	13.01	18.21	16.07	35.01	22.70
131125	5.81	13.01	21.76	16.39	34.41	22.70
140211	4.20	13.06	14.05	16.41	25.83	22.73
140406	4.03	13.02	12.88	16.39	24.44	22.71
140605	3.87	13.01	10.67	16.40	21.61	22.72
140827	4.19	12.90	9.59	16.67	20.90	22.60
141012	4.65	13.00	7.62	16.37	20.95	22.71
141219	4.27	13.03	4.64	16.79	16.74	22.73
150209	5.41	13.00	5.52	17.28	19.02	22.69
150417	5.31	13.03	5.62	17.67	18.07	22.71
150610	6.56	12.98	7.39	17.65	22.52	22.72
150817	5.70	12.91	5.85	17.53	19.80	22.59
151005	6.78	13.00	6.44	17.65	24.78	22.70
151213	5.72	13.01	4.89	17.66	21.69	22.70
160215	5.93	12.61	4.34	17.64	21.20	22.71
160405	5.61	12.65	3.54	17.64	19.25	22.71
160921	6.03	13.05	3.73	17.68	25.14	22.72
161120	8.59	13.04	5.43	17.64	33.31	22.71
170131	9.08	13.01	5.35	17.68	30.64	22.69
170415	9.35	13.01	5.11	17.67	29.85	22.69
170604	7.98	13.02	3.99	17.65	25.87	22.70
170828	5.51	13.00	2.85	17.64	20.51	22.72
171101	4.23	13.01	2.18	17.62	15.56	22.71
180102	4.78	13.01	2.01	17.23	15.29	22.72
180310	6.07	13.10	2.22	17.33	15.56	22.80
180615	9.15	13.12	3.55	17.34	20.73	22.79
180910	11.00	13.11	5.56	17.33	25.19	22.81
181103	15.57	13.10	8.36	17.75	33.03	22.81
190105	15.06	13.12	7.78	17.75	26.66	22.80

presented the different locations of these four transition SiO masers based on the KVN VLBI observations. They reported that the 42.8 GHz SiO maser stems from the innermost region with a ring radius of 13.31 mas, i.e., inside the 43.1 GHz SiO maser (ring radius = 13.63 mas); the 86.2 GHz SiO maser (ring radius = 14.10 mas) stems from the outer region of the 43.1 GHz SiO maser; and the 129.3 GHz SiO maser (ring radius = 16.08 mas) is located in the outermost region from the center of VX Sgr. Su et al. (2012) showed that the 42.8 GHz SiO maser is emitted from slightly inside of the 43.1 GHz SiO maser in the third epoch, and according to the high-resolution VLBA observations toward VX Sgr, they overlap each other in the last two epochs. This overlap of the 43.1 and 42.8 GHz SiO masers validates the similar properties of the 43.1 and 42.8 GHz SiO masers in the model result of Gray & Humphreys (2000), wherein the 43.1 GHz SiO maser appears over a wider region than the 42.8 GHz SiO maser. For the different locations between the 43.1 and 86.2 GHz SiO masers, the model by Gray et al. (2009), wherein the 86.2 GHz SiO maser occurs at larger radii than the 43.1 GHz SiO maser, supports the above results of Yoon et al. (2018). However, the model by Gray et al. (2018) did not afford the spatial distribution of the 129.3 GHz SiO maser spots. For the pumping mechanism of the 129.3 GHz SiO maser, Yoon et al. (2018) suggested that radiative pumping works based on the optical phase dependency of the ring size of the 129.3 GHz SiO maser. A detailed discussion of the characteristics of the four SiO transition maser lines will be provided in the next paper on the KVN VLBI monitoring observations of the SiO and H_2O masers.

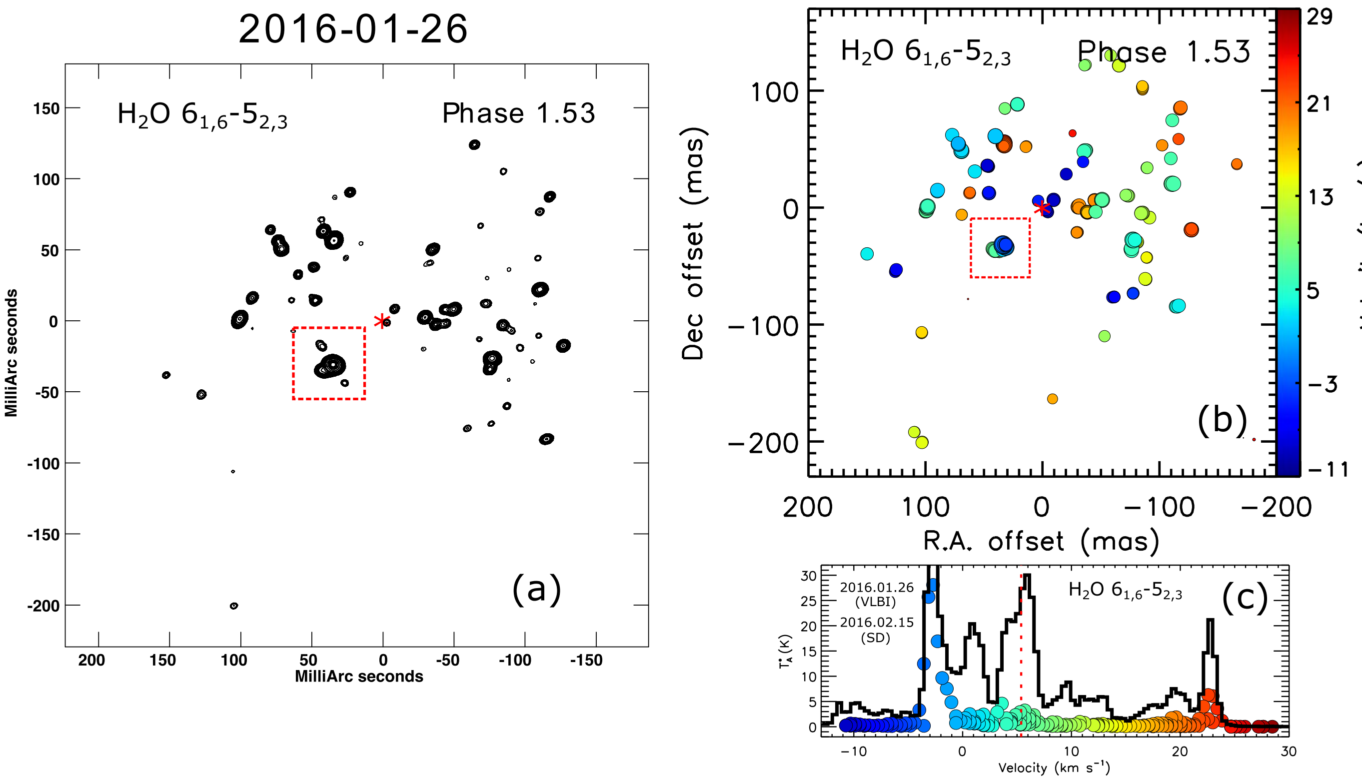

Figure 12. The VLBI observations of the H_2O maser on 2016 January 26 ($\phi = 1.53$). (a) Moment zero map, (b) position–velocity spot map, and (c) recovered spectrum from the velocity-dependent maser spots superposed on the single-dish spectrum on 2016 February 15 ($\phi = 1.56$) in Figure 10. The red dotted line in panel (c) represents the stellar velocity ($V_* = 5.3$ km s^{-1}). The strongest features in the −6 to 3 km s^{-1} velocity range are mostly located in the red dotted square in panels (a) and (b). The color of the spots indicates the local standard of rest velocity in panels (b) and (c), and the size of the spot is a logarithmic scale of the intensity in panel (b). The red asterisk denotes the position of VX Sgr determined by the ring fitting of the SiO masers (Yoon et al. 2018).

6. Summary

We performed simultaneous monitoring observations of the 22.2 GHz ($6_{1,6}$–$5_{2,3}$) H_2O and 43.1/42.8/86.2/129.3 GHz ($v = 1$, $J = 1$–0, $v = 2$, $J = 1$–0, $v = 1$, $J = 2$–1, $J = 3$–2) SiO masers toward the red supergiant VX Sgr using the KVN single-dish telescope. Monitoring was performed about every 2 months from 2013 May to 2019 January (in a total of 30 epochs) except maintenance season, including four optical maxima in the active phase of the light curve of the AAVSO optical pulsation cycles. We investigated the variation characteristics of H_2O and SiO maser properties according to the stellar pulsation phases; they are summarized as follows.

1. The line profile of the H_2O maser always comprises various velocity components with a wider velocity range (−16.2 to 25.5 km s^{-1}) than that of the SiO maser (−8.1 to 19.7 km s^{-1}). The peak velocities of the H_2O maser vary from highly redshifted to blueshifted velocities with respect to the stellar velocity during our monitoring observations (Figures 2 and 3). On the other hand, most peak velocities of SiO masers appear around the stellar velocity (Figures 6 and 7).
2. The intensity variations of the H_2O and SiO masers exhibit different characteristics based on each maser transition line. The peak intensity of the H_2O maser is correlated with the optical light curve with a certain phase delay (0.26) of the first optical maximum. However, there is a missing intensity maximum of the H_2O maser corresponding to the second optical maximum. The peak intensities of the 43.1 and 42.8 GHz SiO masers also appear after the optical maxima with a certain phase delay, but missing maxima appear corresponding to the third optical maximum. They gradually increase during the third optical period. The peak intensities of the 86.2 and 129.3 GHz SiO masers exhibit a weak maximum corresponding to each optical maximum and exhibit different patterns compared to the 43.1 and 42.8 GHz masers. The integrated intensity variations of the H_2O and SiO masers show a tendency similar to the peak intensity variations.
3. The peak and mean velocities of the H_2O maser sustain a relatively constant velocity around the stellar velocity and display a blueshift in most phases compared to those of the SiO masers. However, the peak and mean velocities of the SiO masers show large fluctuations around the stellar velocity. Additionally, the peak velocities of the 43.1 and 42.8 GHz SiO masers exhibit an increasing trend to redshifted velocities with respect to the stellar velocity from the second optical maximum. In contrast, those of the 86.2 and 129.3 GHz SiO masers exhibit a different pattern: mainly blueshifted velocities with respect to the stellar velocity.
4. The peak intensities of the H_2O masers are always larger than those of the SiO masers, except for the 86.2 GHz SiO and H_2O masers in 2015 April (Figure 7(a)). The peak intensity ratios of the SiO to H_2O masers show a maximum around the second optical maximum. However, these ratios display a maximum before the fourth optical maximum in the 43.1, 42.8, and 86.2 GHz SiO

masers. This maximum around the second optical maximum seems to be caused by the missing maximum of the H_2O maser around the second optical maximum.

5. The relations among the peak intensities of the 11 detail components in the single-dish line profile of the H_2O maser and pulsation phases were examined in Figure 11. The peak intensities of most components correlate well with the pulsation phases. The peak velocity variations of the 11 components over time were also examined. The peak velocities of the components gradually decreased or increased with respect to the stellar velocity during the monitoring observations, implying an accelerating motion (line-of-sight direction -0.67 and 0.87 km s^{-1} yr^{-1} depending on the components) and development of asymmetries in the H_2O maser region. The average expansion velocity measured by half of the FWZPs of the H_2O masers is 20.8 km s^{-1}, which does not reach the terminal velocity of 26 km s^{-1} and still accelerates.
6. The single-dish spectrum of the H_2O maser on 2016 February 15 ($\phi = 1.56$) was compared with the VLBI monitoring results on 2016 January 26 ($\phi = 1.53$) in Figure 12, which is the closest to the single-dish observation date. Strong -6 to 3 km s^{-1} components in the single-dish spectrum were present southeast of the stellar position (Figure 12). Thus, the interaction between an outflow and surrounding materials in the southeast region is a dominant factor for the strongest maser pumping of the H_2O maser.

This work was supported by the Basic Science Research Program through the National Research Foundation of Korea (NRF) funded by the Ministry of Education (D.-H.Y.; NRF-2019R1A6A3A01091901), by the National Research Foundation of Korea (NRF) funded by the Korea government (MSIT) (S.-H.C.; No. 2022R1A2C1091317), and by the Major Project Research Fund (2018–2020) of the Korea Astronomy and Space Science Institute (KASI). We are grateful to all the staff members at KVN who helped operate the array and the single-dish telescope and correlate the data. KVN is a facility operated by KASI, which is under the protection of the National Research Council of Science and Technology (NST). KVN operations are supported by the Korea Research Environment Open Network (KREONET), which is managed and operated by the Korea Institute of Science and Technology Information (KISTI).

ORCID iDs

Dong-Hwan Yoon https://orcid.org/0000-0001-7120-8851
Se-Hyung Cho https://orcid.org/0000-0002-2012-5412
Haneul Yang https://orcid.org/0000-0001-6493-0619
Youngjoo Yun https://orcid.org/0000-0002-0822-2973
Jaeheon Kim https://orcid.org/0000-0001-9825-7864

References

Alcolea, J., Pardo, J. R., Bujarrabal, V., et al. 1999, A&AS, 139, 461
Berulis, I. I., Pashchenko, M. I., & Rudnitskij, G. M. 1999, A&AT, 18, 77
Bujarrabal, V. 1994, A&A, 285, 953
Chapman, J. M., & Cohen, R. J. 1986, MNRAS, 220, 513
Chen, X., Shen, Z.-Q., Imai, H., & Kamohara, R. 2006, ApJ, 640, 982
Chen, X., Shen, Z.-Q., & Xu, Y. 2007, ChJAA, 7, 531
Chiavassa, A., Lacour, S., Millour, F., et al. 2010, A&A, 511, A51
Cho, C.-Y., Cho, S.-H., Kim, S., et al. 2017, ApJS, 232, 13
Cho, S.-H., & Kim, J. 2012, AJ, 144, 129
Cho, S.-H., Yun, Y., Kim, J., et al. 2018, in IAU Symp. 336, Astrophysical Masers: Unlocking the Mysteries of the Universe (Cambridge: Cambridge Univ. Press), 359
Cooke, B., & Elitzur, M. 1985, ApJ, 295, 175
Diamond, P. J., Kemball, A. J., Junor, W., et al. 1994, ApJL, 430, L61
Gomez Balboa, A. M., & Lepine, J. R. D. 1986, A&A, 159, 166
Gonzalez-Alfonso, E., Cernicharo, J., Alcolea, J., et al. 1998, A&A, 334, 1016
Gray, M. D., & Humphreys, E. M. L. 2000, NewA, 5, 155
Gray, M. D., Mason, L., & Etoka, S. 2018, MNRAS, 477, 2628
Gray, M. D., Wittkowski, M., Scholz, M., et al. 2009, MNRAS, 394, 51
Han, S.-T., Lee, J.-W., Kang, J., et al. 2008, IJIMW, 29, 69
Kamohara, R., Deguchi, S., Miyoshi, M., & Shen, Z.-Q. 2005, PASJ, 57, 341
Kim, J., Cho, S.-H., & Kim, S. J. 2013, AJ, 145, 22
Kim, J., Cho, S.-H., & Kim, S. J. 2014, AJ, 147, 22
Kim, J., Cho, S.-H., Oh, C. S., & Byun, D.-Y. 2010, ApJS, 188, 209
Kiss, L. L., Szabo, G. M., & Bedding, T. R. 2006, MNRAS, 372, 1721
Lockett, P., & Elitzur, M. 1992, ApJ, 399, 704
Lockwood, G. W., & Wing, R. F. 1982, MNRAS, 198, 385
Murakawa, K., Yates, J. A., Richards, A. M. S., & Cohen, R. J. 2003, MNRAS, 344, 1
Pardo, J. R., Alcolea, J., Bujarrabal, V., et al. 2004, A&A, 424, 145
Samus, N. N., Kazarovets, E. V., Durlevich, O. V., et al. 2009, yCat, B/gcvs
Samus, N. N., Kazarovets, E. V., Durlevich, O. V., Kireeva, N. N., & Pastukhova, E. N. 2017, ARep, 61, 80
Su, J. B., Shen, Z.-Q., Chen, X., et al. 2012, ApJ, 754, 47
Su, J. B., Shen, Z.-Q., Chen, X., & Jiang, D. R. 2018, ApJ, 853, 42
Tabernero, H. M., Dorda, R., Negueruela, I., & Marfil, E. 2021, A&A, 646, A98
Vlemmings, W. H. T., van Langevelde, H. J., & Diamond, P. J. 2005, A&A, 434, 1029
Xu, S., Zhang, B., Reid, M. J., et al. 2018, ApJ, 859, 14
Yang, H., Cho, S.-H., Yun, Y., et al. 2020, MNRAS, 495, 1284
Yoon, D.-H., Cho, S.-H., Kim, J., Yun, Y. j., & Park, Y.-S. 2014, ApJS, 211, 15
Yoon, D.-H., Cho, S.-H., Yun, Y., et al. 2018, NatCo, 9, 2534
Yun, Y. J., & Park, Y.-S. 2012, A&A, 545, A136